

Longitudinal multi-omic signatures of ARDS and sepsis inflammatory phenotypes identify pathways associated with mortality

Narges Alipanah-Lechner, Lucile Neyton, Pratik Sinha, Carolyn Leroux, Kim Bardillon, Sidney A. Carrillo, Suzanna Chak, Olivia Chao, Taarini Hariharan, Carolyn Hendrickson, Kirsten Kangelaris, Charles R. Langelier, Deanna Lee, Chelsea Lin, Kathleen Liu, Liam Magee, Angelika Ringor, Aartik Sarma, Emma Schmiege, Natasha Spottiswoode, Kathryn Sullivan, Melanie F. Weingart, Andrew Willmore, Hanjing Zhuo, Angela J. Rogers, Kathleen A. Stringer, Michael A. Matthay, Carolyn S. Calfee

J Clin Invest. 2025. <https://doi.org/10.1172/JCI196290>.

Clinical Research and Public Health In-Press Preview Clinical Research Inflammation Pulmonology

BACKGROUND. Critically ill patients with acute respiratory distress syndrome (ARDS) and sepsis exhibit distinct inflammatory phenotypes with divergent clinical outcomes, but the underlying molecular mechanisms remain poorly understood. These phenotypes, derived from clinical data and protein biomarkers, were associated with metabolic differences in a pilot study.

METHODS. We performed integrative multi-omics analysis of blood samples from 160 ARDS patients in the ROSE trial, randomly selecting 80 patients from each latent class analysis-defined inflammatory phenotype (Hyperinflammatory and Hypoinflammatory) with phenotype probability >0.9. Untargeted plasma metabolomics and whole blood transcriptomics at Day 0 and Day 2 were analyzed using multi-modal factor analysis (MEFISTO). The primary outcome was 90-day mortality, with validation in an independent critically ill sepsis cohort (EARLI).

RESULTS. Multi-omics integration revealed four molecular signatures associated with mortality: (1) enhanced innate immune activation coupled with increased glycolysis (associated with Hyperinflammatory phenotype), (2) hepatic dysfunction and immune dysfunction paired with impaired fatty acid beta-oxidation (associated with Hyperinflammatory phenotype), (3) interferon program suppression coupled with altered mitochondrial respiration (associated with Hyperinflammatory phenotype), and (4) redox impairment and cell proliferation pathways (not associated with inflammatory phenotype). These signatures persisted through Day 2 of trial enrollment. Within-phenotype analysis revealed distinct mortality-associated pathways in each group. All molecular signatures were validated in the independent EARLI cohort.

CONCLUSIONS. Inflammatory phenotypes of ARDS reflect distinct underlying biological processes [...]

Find the latest version:

<https://jci.me/196290/pdf>



1 **Title:** Longitudinal multi-omic signatures of ARDS and sepsis inflammatory phenotypes identify
2 pathways associated with mortality

3

4 **Authors:** Narges Alipanah-Lechner^{1*†}, Lucile Neyton^{1†}, Pratik Sinha², Carolyn Leroux¹, Kim
5 Bardillon³, Sidney A. Carrillo¹, Suzanna Chak³, Olivia Chao³, Taarini Hariharan¹, Carolyn
6 Henrickson⁴, Kirsten Kangelaris⁵, Charles R. Langelier⁶, Deanna Lee³, Chelsea Lin¹, Kathleen
7 Liu^{7,8}, Liam Magee³, Angelika Ringor³, Aartik Sarma¹, Emma Schmiege¹, Natasha
8 Spottiswoode⁶, Kathryn Sullivan¹, Melanie F. Weingart¹, Andrew Willmore¹, Hanjing Zhuo³,
9 Angela J. Rogers⁹, Kathleen A. Stringer^{10,11}, Michael A. Matthay^{1,8}, Carolyn S. Calfee^{1,8}

10

11 **Affiliations:**

- 12 1. Division of Pulmonary, Critical Care, Allergy, and Sleep Medicine, Department of
13 Medicine, University of California San Francisco; USA
- 14 2. Division of Clinical and Translational Research, Department of Anesthesia, Washington
15 University School of Medicine; St. Louis, Missouri, USA
- 16 3. Cardiovascular Research Institute, University of California San Francisco; USA
- 17 4. Division of Pulmonary and Critical Care, Department of Medicine, Zuckerberg San
18 Francisco General Hospital; California, USA
- 19 5. Division of Hospital Medicine, Department of Medicine, University of California San
20 Francisco; USA
- 21 6. Division of Infectious Disease, Department of Medicine, University of California San
22 Francisco; USA

- 23 7. Division of Nephrology, Department of Medicine, University of California San
24 Francisco; USA
- 25 8. Department of Anesthesia, University of California San Francisco; USA
- 26 9. Division of Pulmonary and Critical Care, Department of Medicine, Stanford University;
27 California, USA
- 28 10. Department of Clinical Pharmacy, College of Pharmacy, University of Michigan; USA
- 29 11. Division of Pulmonary and Critical Care Medicine, School of Medicine, University of
30 Michigan; USA

31

32 * Corresponding author:

33 Narges Alipanah-Lechner, MD MAS

34 513 Parnassus Ave.

35 HSE716

36 San Francisco, CA 94143

37 Telephone: 714-507-5553

38 Email: narges.alipanah@ucsf.edu.

39

40 † These authors contributed equally to this work and share the first author position.

41

42 **Conflict-of-interest statement:** The authors have declared that no conflict of interest exists.

43

44 **Word Count: 10,695**

45

46 **Abstract**

47

48 **Background:** Critically ill patients with acute respiratory distress syndrome (ARDS) and sepsis
49 exhibit distinct inflammatory phenotypes with divergent clinical outcomes, but the underlying
50 molecular mechanisms remain poorly understood. These phenotypes, derived from clinical data
51 and protein biomarkers, were associated with metabolic differences in a pilot study.

52

53 **Methods:** We performed integrative multi-omics analysis of blood samples from 160 ARDS
54 patients in the ROSE trial, randomly selecting 80 patients from each latent class analysis-defined
55 inflammatory phenotype (Hyperinflammatory and Hypoinflammatory) with phenotype
56 probability >0.9. Untargeted plasma metabolomics and whole blood transcriptomics at Day 0 and
57 Day 2 were analyzed using multi-modal factor analysis (MEFISTO). The primary outcome was
58 90-day mortality, with validation in an independent critically ill sepsis cohort (EARLI).

59

60 **Results:** Multi-omics integration revealed four molecular signatures associated with mortality:
61 (1) enhanced innate immune activation coupled with increased glycolysis (associated with
62 Hyperinflammatory phenotype), (2) hepatic dysfunction and immune dysfunction paired with
63 impaired fatty acid beta-oxidation (associated with Hyperinflammatory phenotype), (3)
64 interferon program suppression coupled with altered mitochondrial respiration (associated with
65 Hyperinflammatory phenotype), and (4) redox impairment and cell proliferation pathways (not
66 associated with inflammatory phenotype). These signatures persisted through Day 2 of trial
67 enrollment. Within-phenotype analysis revealed distinct mortality-associated pathways in each
68 group. All molecular signatures were validated in the independent EARLI cohort.

69

70 **Conclusions:** Inflammatory phenotypes of ARDS reflect distinct underlying biological processes
71 with both phenotype-specific and phenotype-independent pathways influencing patient
72 outcomes, all characterized by mitochondrial dysfunction. These findings suggest potential
73 therapeutic targets for precise treatment strategies in critical illness.

74

75 **Funding:** This work is the result of NIH funding (National Heart Lung and Blood Institute
76 grants K23HL173669 [NA], R35HL140026 and R35177135 [CSC]; National Institute of
77 General Medical Sciences grant R35GM136312 [KAS]) and is subject to the NIH Public Access
78 Policy. Through acceptance of this federal funding, the NIH has been given a right to make the
79 work publicly available in PubMed Central.

80

81

82 INTRODUCTION

83

84 The acute respiratory distress syndrome (ARDS) and sepsis are devastating critical illness
85 syndromes with unacceptably high mortality rates approaching 40-50% in the United States (1,
86 2). A significant challenge to developing effective treatments has been the marked heterogeneity
87 in clinical presentation, underlying biology, and treatment responses among affected patients (3,
88 4).

89

90 Recent advances in molecular phenotyping have identified reproducible subgroups of ARDS and
91 sepsis patients with distinct pathobiology. Latent class analyses (LCA) of clinical and plasma
92 protein data consistently reveal two predominant phenotypes: a “Hyperinflammatory” phenotype
93 characterized by elevated plasma inflammatory protein biomarkers, shock, and higher mortality,
94 and a “Hypoinflammatory” phenotype with relatively lower inflammatory protein biomarkers
95 and better outcomes (5-10). These phenotypes, identified across multiple ARDS and sepsis
96 cohorts, demonstrate differential therapeutic responses in secondary analyses of randomized
97 trials, suggesting they represent endotypes with distinct disease mechanisms (5, 11, 12). Clinical
98 trials incorporating prospective phenotyping are being developed, including the PANTHER trial,
99 which will start enrolling in mid-2025 (13). However, the biological processes driving each
100 phenotype and mechanisms underlying unfavorable outcomes within each phenotype remain
101 poorly understood. While protein biomarker studies have provided valuable insights into
102 inflammatory patterns, they capture only a small fraction of the complex molecular landscape.
103 Previous metabolic profiling of 93 patients with ARDS demonstrated that the
104 Hyperinflammatory phenotype exhibits reduced circulating lipids and a glycolytic shift, while

105 transcriptomic analyses revealed increased expression of genes related to the innate immune
106 response, tissue remodeling, and reduced interferon signaling (10, 14). However, isolated -omic
107 approaches may miss critical interactions between cellular programming and systemic
108 metabolism essential for understanding disease processes and treatment responses.

109

110 In this study, we applied longitudinal multi-omics profiling to characterize the molecular basis of
111 ARDS/sepsis inflammatory phenotypes and identify mechanisms associated with poor outcomes.
112 We hypothesized that these phenotypes would demonstrate distinct metabolic profiles and that
113 integrated metabolomic-transcriptomic analysis would reveal novel outcome-associated
114 mechanisms with therapeutic potential. By simultaneously measuring the metabolome and
115 transcriptome at two timepoints in a large ARDS cohort, we aimed to: (1) identify metabolic
116 differences between inflammatory phenotypes, (2) characterize coordinated metabolomic-
117 transcriptomic signatures contributing to heterogeneity, (3) determine temporal stability of these
118 patterns, and (4) uncover potentially targetable pathways associated with mortality. This
119 comprehensive molecular characterization aims to advance our understanding of ARDS/sepsis
120 heterogeneity and identify therapeutic approaches tailored to specific patient subgroups.

121

122

123 **RESULTS**

124

125 **LCA phenotypes have distinct metabolic profiles**

126

127 We first asked whether ethylenediaminetetraacetic acid (EDTA) plasma metabolites would be
128 different between latent class analysis (LCA)-defined ARDS phenotypes. We evaluated patients
129 from the ROSE trial of neuromuscular blockade for the treatment of moderate-to-severe ARDS
130 (Figure 1A), who had previously undergone LCA phenotyping using plasma protein biomarkers
131 and clinical variables (10, 15). We randomly selected 80 patients in each phenotype with high
132 phenotype membership probability (>0.9) (Supplemental Figure 1). These 160 total patients had
133 a median age of 58.5 (IQR 47 to 68), were predominantly male (64%), and were racially
134 designated as white (78%), with equivalent proportions randomized to neuromuscular blockade
135 across phenotypes (Supplemental Table 1). The Hyperinflammatory group exhibited lower
136 median body mass index (BMI), higher APACHEIII scores, reduced glomerular filtration rate
137 (GFR), and higher prevalence of comorbid liver disease and leukemia. Corticosteroid
138 administration rates were identical between phenotypes (24%). Consistent with previous studies,
139 Hyperinflammatory patients more frequently required vasopressors at enrollment (86% vs 21%),
140 experienced more than twice the mortality at 28 and 90 days (61% vs 24%), and had
141 significantly fewer ventilator-, ICU-, and hospital-free days. Pneumonia was the predominant
142 ARDS etiology in both phenotypes, while all patients with extrapulmonary sepsis-induced ARDS
143 belonged to the Hyperinflammatory group.

144

145 Untargeted metabolic profiling identified 1,378 known metabolites (Supplemental Figure 2).
146 After removing metabolites with high missingness (>25%), 982 remained for analysis.
147 Differential abundance analysis using limma with adjustment for potential confounders identified
148 541 metabolites significantly different between phenotypes at Day 0, with substantial differences
149 across all metabolic classes (Figure 2, A and B). Similar analysis at Day 2 revealed 494
150 significantly different metabolites, largely overlapping with Day 0 findings (Figure 2C).
151 Metabolite enrichment analysis using Metabolon's library highlighted 60 dysregulated pathways
152 at Day 0 and 56 at Day 2, totaling 74 unique metabolic pathways (Figure 2D, Supplemental
153 Figure 3). The top 20 most differentially abundant metabolites belonged to lipids and amino acid
154 classes, though the highest proportion of differentially abundant metabolites were related to
155 energy production at both timepoints (Supplemental Tables 2 and 3). The primary metabolic
156 differences between phenotypes persisted in sensitivity analyses restricted to pneumonia-only
157 patients and adjusting for shock (Supplemental Figure 4, Supplemental Tables 4 and 5).
158 Similarly, adjusting for renal replacement therapy did not meaningfully alter the metabolomic
159 differences between phenotypes (Supplemental Figure 5, Supplemental Tables 6 and 7).
160
161 In patients surviving through Day 2, individual metabolite trajectories did not differ by 90-day
162 mortality in the full cohort or within phenotypes (Supplemental Figure 6). However, when
163 metabolites were aggregated by class, several metabolic classes demonstrated significantly
164 different trajectories based on 90-day mortality (Supplemental Figure 7A). Tryptophan
165 metabolism, steroid pathways, and gamma-glutamyl amino acids increased over time in non-
166 survivors, who also demonstrated decreasing levels of lactosylceramides, lysoplasmalogens,
167 hexosylceramides, sphingolipids, phospholipids, and ascorbate/aldarate metabolites.

168 Hypoinflammatory non-survivors had increasing progestin steroids (Supplemental Figure 7B),
169 while Hyperinflammatory non-survivors exhibited decreasing acyl carnitines, plasmalogens, and
170 ascorbate/aldarate metabolites alongside rising pregnenolone steroids (Supplemental Figure 7C).
171 Testing for sex interactions across all metabolites revealed no biologically meaningful sex-
172 specific differences in mortality-related trajectories (Supplemental Figure 8).

173

174 **Mitochondrial metabolites are associated with Hyperinflammatory phenotype and** 175 **mortality**

176 We hypothesized that observed derangements in fatty acid oxidation, lactoyl amino acids, and
177 TCA metabolites stemmed from mitochondrial dysfunction. To test this hypothesis, we curated
178 mitochondria-associated metabolites based on established circulating biomarkers in genetic
179 mitochondrial disorders (16). Of 38 detectable mitochondria-associated metabolites in our
180 cohort, 37 (97%) differed significantly between phenotypes (Figure 3A). Since vasopressors can
181 enhance glycolysis and lactate production (17, 18), we investigated whether increased
182 mitochondrial metabolic activity in the Hyperinflammatory group merely reflected vasopressor
183 administration. Differential abundance analysis incorporating vasopressor administration (≥ 1
184 hour infusion in preceding 24 hours) as a covariate revealed that 31 (81%) mitochondrial
185 metabolites remained differentially abundant between phenotypes (Figure 3A), suggesting the
186 distinct mitochondrial signature in the Hyperinflammatory phenotype is independent of
187 vasopressor effects. Further examining metabolic mitochondrial function through plasma redox-
188 coupled (e.g., NADH/NAD⁺) metabolite pairs (19-23), we observed both lactate:pyruvate and 3-
189 hydroxybutyrate:acetoacetate ratios were significantly higher in Hyperinflammatory patients
190 (Figure 3B), indicating systemic redox imbalance. Finally, assessing clinical relevance, 26 of 38

191 mitochondrial metabolites (68%) were associated with 90-day mortality in multivariate logistic
192 regression models (Figure 3C).

193

194 As proof of concept that metabolic differences identified through untargeted profiling reflected
195 clinically quantifiable phenotype distinctions, we tested whether clinical lactate values differed
196 by phenotype. Since ROSE lacked clinical lactate data, we examined measurements from
197 EARLI, an independent cohort of critically ill sepsis patients who had undergone LCA
198 phenotyping (24). While both phenotypes presented with elevated lactate levels,
199 hyperinflammatory patients had persistently higher lactate throughout nearly the entire follow-up
200 period (Figure 3, D-F), validating that our metabolomic approach successfully identified
201 clinically meaningful phenotypic differences. To further validate that metabolomic measurements
202 captured patient-level lactate differences, we compared rankings between metabolomic and
203 clinical lactate within EARLI patients with paired measurements available at baseline (n=137).
204 Metabolomic lactate demonstrated strong rank correlation with clinical lactate (Spearman's $\rho =$
205 0.576 , $p < 1 \times 10^{-4}$, Supplemental Figure 9), confirming our untargeted platform reliably captures
206 relative metabolite differences between patients.

207

208 **Multi-omics analysis identifies principal factors related to LCA phenotypes**

209

210 To identify principal sources of biological heterogeneity in the ROSE cohort, we next performed
211 integrated analysis of longitudinal metabolomics and whole blood transcriptomics across all
212 patients (Figure 1B). We selected the top 500 metabolites and 2500 gene transcripts by median
213 absolute deviation in the full cohort for multi-omics analysis (Figure 4A). Applying a MEFISTO

214 (Method for the Functional Integration of Spatial and Temporal Omics data) model incorporating
215 both data types from both timepoints, we used temporal information as a covariate and
216 configured the model to identify 10 latent factors (25). MEFISTO is a dimensionality reduction
217 unsupervised approach for integrating multi-modal data to identify driving sources of variation
218 across data modalities. MEFISTO also disentangles sources of variation that change over time
219 from those that are independent of time. Though MEFISTO does not enforce factor
220 orthogonality, Spearman's correlation analysis revealed no significant inter-factor correlations,
221 confirming each factor captured a distinct source of variability (Figure 4B). The model explained
222 49.6% of the total variance (R^2) in transcriptomic data and 40.6% in metabolomic data
223 (Supplemental Figure 10). Factors 1-3 collectively accounted for 59% of explained
224 transcriptomic variance and 69% of explained metabolomic variance (Figure 4C, Supplemental
225 Table 8). Factor 1 was predominantly driven by transcriptomic data, Factor 2 by metabolomic
226 data, and Factor 3 by both data modalities.

227

228 We next analyzed associations between each latent factor at Day 0 and key clinical
229 characteristics and outcomes. Factors 1-4 exhibited strong associations with LCA phenotype
230 designation, APACHE III scores, and ventilator free days, while demonstrating variable
231 associations with GFR, vasopressor use, corticosteroid administration, and propofol infusion
232 (Figure 4D). The first three factors each explained more than 15% of model variance and were
233 independently associated with mortality. Notably, Factor 5, lacking association with LCA
234 phenotypes, demonstrated strong independent association with mortality. While Factor 2
235 substantially separated phenotypes, the combination of Factors 2 and 3 achieved near-complete
236 phenotype discrimination (Figure 4E). These findings indicate that the principal sources of

237 biological heterogeneity identified through our data-driven multi-omic approach strongly aligned
238 with the biological signals captured by LCA phenotype designation.

239

240 **Multi-omic factors are related to mortality**

241

242 Factors 1, 2, 3 and 5 demonstrated strong associations with mortality (Figure 4D). MEFISTO
243 identified all factors as time-independent (time scales = 0), and the rate of change in factor
244 values over time did not differ by 90-day mortality outcome (Figure 4F). In stepwise logistic
245 regression analysis, a combination of Factors 2 and 3 was sufficient to nullify the relationship
246 between LCA phenotype and mortality (Supplemental Figure 11). Complete enrichment results
247 are provided in the Supplemental Supporting Data Values, with representative examples shown
248 in Figure 5.

249

250 Factor 1, predominantly driven by gene expression, revealed coordinated changes between whole
251 blood transcripts and plasma metabolites, primarily reflecting innate immune activation (Figure
252 5, A-D). To better understand the cellular origins of these transcriptional signatures, we
253 performed computational deconvolution using CIBERSORTx with a published sepsis neutrophil
254 reference dataset.⁽²⁶⁾ Factor 1 demonstrated strong positive correlation with total neutrophils
255 and immature progenitor neutrophils, while showing negative correlation with adaptive immune
256 cells (Supplemental Figure 12A). Gene set enrichment analysis demonstrated significant positive
257 enrichment in neutrophil degranulation, characterized by upregulation of emergency
258 granulopoiesis markers and stress response genes (Supplemental Figure 12B-D), alongside
259 TLR1:TLR2 signaling pathways, glycosaminoglycan (GAG) metabolism, lipid metabolism, and

260 5-eicosatetraenoic acid (5-ETE) synthesis pathways, with negative enrichment in protein
261 synthesis/trafficking and EIF2AK4-mediated integrated stress response pathways. These
262 transcriptional changes accompanied systemic metabolic alterations characterized by decreased
263 plasma levels of long-chain polyunsaturated fatty acids, lysophospholipids, and plasmalogens,
264 coupled with elevated pregnenolone and androgenic steroids, lactoyl amino acids, glycolytic
265 intermediates, and branched chain amino acid catabolites.

266

267 Factor 2, significantly associated with clinical evidence of hepatic and renal dysfunction (Figure
268 4D), was primarily metabolite-driven (Figure 5, E-H). The plasma metabolome demonstrated
269 accumulation of ω -oxidation products (monohydroxy and dicarboxylated fatty acids) alongside
270 decreased membrane-associated lipids and lipid signaling molecules (Figure 5H). Transcriptional
271 profiling revealed increased expression of ABCA1, the cholesterol efflux pump, as well as
272 positive enrichment of translation machinery and EIF2AK4-mediated amino acid stress response
273 pathways (Figure 5F), with negative enrichment in neutrophil degranulation (Supplemental
274 Figure 12), platelet activation, and G-protein coupled receptor signaling pathways.

275 Computational deconvolution revealed that Factor 2 correlated negatively with mature
276 neutrophils and adaptive immune cells, suggesting depletion or functional suppression of these
277 populations (Supplemental Figure 12).

278

279 Factor 3, associated with clinical evidence of renal dysfunction (Figure 4D), was characterized
280 by impaired host response with reduced interferon signaling and increased systemic metabolic
281 stress (Figure 5, I-L). Transcriptional analysis revealed positive enrichment for influenza
282 infection and basic cellular processes including protein synthesis and RNA processing, while

283 immune signaling pathways were broadly suppressed (Figure 5J). Higher Factor 3 values
284 corresponded with increased expression of mitochondrial oxidative phosphorylation genes,
285 particularly complexes I and III. Notably, both Type I and Type II interferon signaling pathways
286 were downregulated, alongside decreased expression of lymphoid cell interaction genes. These
287 transcriptional changes were accompanied by elevated lactoyl amino acids and polyamines, and
288 reduced sphingomyelins and lysophospholipids.

289

290 Factor 5 values were significantly associated with mortality but not LCA phenotype (Figure 4D).
291 Analysis revealed a molecular state characterized by cell proliferation and oxidative stress
292 (Figure 4, M-P). Transcriptional profiling demonstrated positive enrichment of DNA replication,
293 cell cycle progression, RUNX1-mediated hematopoietic differentiation and megakaryocyte
294 activation, HCMV infection, and increased WNT target gene engagement (Figure 5N). This
295 hyperproliferative state featured increased expression of mitochondrial iron homeostasis genes,
296 Fe-S protein metabolism, and ROS management systems, concurrent with activation of oxidative
297 stress-induced senescence pathways.

298

299 **Multi-omics analysis reveals mortality-associated signatures within LCA phenotypes**

300

301 To investigate mechanisms underlying outcome heterogeneity within each ARDS phenotype, we
302 conducted separate multi-omics factor analyses within each phenotype (Figure 1C). Using
303 MEFISTO with identical parameters to our full cohort analysis, we found that, in both
304 phenotypes, transcriptional variation contributed more substantially to within-phenotype
305 heterogeneity than metabolomic variation (Figure 6, A and B; Figure 7, A and B).

306

307 In the Hypoinflammatory group, Factor 1, primarily characterized by gene expression patterns,
308 was associated with mortality (Figure 6, B and C). Factor 1 values demonstrated no differential
309 change over time based on survival status (Figure 6D) but had strong association with moderate-
310 to-high dose corticosteroid treatment in the preceding 24 hours. Gene expression profiling
311 revealed positive enrichment of innate immune response pathways (neutrophil degranulation and
312 IL1 signaling) with concurrent negative enrichment of translation machinery, starvation
313 response, nonsense mediated decay, viral infection, adaptive immune response, and integrated
314 stress response pathways amongst others (Figure 6, E and F).

315

316 In the Hyperinflammatory group, Factors 1-3 explained most data variance (Figure 7B). While
317 Factor 1 had no association with clinical variables, Factor 3 demonstrated strong association with
318 mortality, with similar temporal trajectories between survivors and non-survivors (Figure 7, C
319 and D). Factor 3 was characterized by elevated expression of genes involved in RUNX1
320 mediated hematopoiesis and megakaryopoiesis, epigenetic remodeling, viral infection signatures,
321 and increased cell cycle activity with negative enrichment in transcriptional regulation by
322 VENTX, and TNF receptor superfamily mediating non-canonical NF-kB pathways (Figure 7, E
323 and G). TCA cycle intermediates and mitochondrial metabolites (malate, succinate, fumarate,
324 lactate) were positively weighted (Figure 7F). Metabolite analysis identified systemic stress
325 markers (lactoyl amino acids), altered lipid metabolism, and reduced long chain polyunsaturated
326 fatty acids among others (Figure 7H).

327

328 **Multi-omic signatures are validated in external cohorts**

329

330 To assess generalizability of MEFISTO latent factors derived from our cohort with extreme
331 phenotype designations, we examined these associations in EARLI, an ongoing prospective
332 observational cohort study of critically ill adults with sepsis (Figure 1D). A subset of EARLI
333 patients meeting sepsis criteria within two days of enrollment (n = 818) had previously
334 undergone LCA phenotyping (24). Metabolomic data were available for 195 patients, whole
335 blood transcriptomics for 196 patients, and both data types for 61 patients (Supplemental Figure
336 13, Supplemental Table 9) (27, 28).

337

338 To project ROSE MEFISTO factors onto EARLI patients, we selected the top 100 highest-
339 weighted features by absolute scaled weight within each factor of interest, yielding two
340 transcriptomic signatures (Factors 1 and 3), and one metabolomic signature (Factor 2). This
341 approach reduced noise from lower-weighted features and enabled testing in a larger cohort. We
342 calculated Factor 1 and 3 scores for EARLI patients with transcriptomic data (n=196) and Factor
343 2 values for those with metabolomic data (n=195). All three ROSE MEFISTO factors
344 demonstrated similar LCA phenotype associations in EARLI, with improved phenotype
345 discrimination achieved by combining Factors 2 and 3 (Figure 8, A-C). The four mortality-
346 associated ROSE MEFISTO factors were similarly associated with mortality in EARLI (Figure
347 8D).

348

349 Using the same approach, we projected ROSE MEFISTO mortality-associated factors derived
350 within each LCA phenotype onto the EARLI participants with high phenotype probability (p >
351 0.9). The top 100 features in each phenotype-specific factor yielded one transcriptomic signature

352 per phenotype. Among patients with phenotype probability >0.9 , transcriptomic data were
353 available for 101 with Hypoinflammatory and 61 with Hyperinflammatory sepsis. Both
354 phenotype-specific mortality signatures demonstrated significant mortality associations in the
355 EARLI cohort (Figure 8E).

356

357

358 **DISCUSSION**

359

360 In this integrated multi-omic analysis of ARDS inflammatory phenotypes, we identified distinct
361 transcriptional and metabolomic signatures that differentiate Hyperinflammatory from
362 Hypoinflammatory phenotypes and are associated with clinical outcomes. Three key insights
363 emerged: First, the Hyperinflammatory phenotype exhibits profound mitochondrial dysfunction
364 and metabolic derangement associated with mortality, persisting independently of vasopressor
365 use, suggesting an intrinsic phenotypic feature. Second, longitudinal multi-omic integration
366 revealed four mortality-associated molecular factors representing distinct pathobiological
367 processes: (1) innate immune activation with enhanced glycolysis, (2) hepatic dysfunction
368 coupled with impaired fatty acid oxidation, (3) suppressed interferon signaling with altered
369 mitochondrial respiration, and (4) immune cell proliferation with redox stress. Third, we
370 identified biological signals associated with mortality within each inflammatory phenotype and
371 quantified their relative contribution to overall biological heterogeneity and temporal evolution.
372 These molecular signatures were replicated in an independent cohort of critically ill patients with
373 sepsis, indicating their generalizability. Together, these findings advance our understanding of
374 ARDS and sepsis heterogeneity and identify potential therapeutic targets for phenotype-specific
375 interventions.

376

377 Factor 1, accounting for the largest proportion of molecular variation (35% transcriptomic, 10%
378 metabolomic variance), reveals crucial insights into the relationship between inflammation and
379 outcomes in ARDS. This Factor represents an enhanced innate immune response through
380 neutrophil activation and TLR1:TLR2 signaling, coupled with hypermetabolism. The increased

381 expression of genes related to synthesis of inflammatory mediators (5-ETE) combined with
382 reduced plasma PUFA levels suggest active consumption of circulating lipids, likely to support
383 increased energy demands of expanding immune cell populations and generation of lipid
384 mediators. Glycosaminoglycan (GAG) metabolism enrichment suggests tissue remodeling and
385 altered barrier function, while elevated lactoyl amino acids and increased glycolysis suggest
386 widespread mitochondrial metabolic stress and potential Warburg effect, or aerobic glycolysis, as
387 this factor was independent of hypoxia status (PaO₂:FiO₂) (16, 29). Together, these findings
388 suggest a coordinated systemic response where circulating immune cells undergo inflammatory
389 expansion with corresponding metabolic adaptation via increased glycolysis and lipid
390 metabolism. While our observational data cannot establish whether metabolic disturbances drive
391 immune activation or vice versa, existing literature indicates these relationships are likely
392 bidirectional. Metabolic conditions can modulate immune cell gene expression through
393 epigenetic modifications and transcription factor activation, while immune cell activation drives
394 metabolic reprogramming through altered enzyme expression and activity (30-34). For instance,
395 neutrophil activation involves glycolytic reprogramming to support effector functions, while
396 metabolites like lactate and succinate can directly influence immune cell gene transcription and
397 inflammatory responses through HIF1- α and other metabolic sensors (31, 35-37). Notably,
398 Factor 1 had the weakest association with mortality, suggesting that interventions solely targeting
399 broad suppression of inflammatory responses may be insufficient to fundamentally reduce
400 mortality related to ARDS and sepsis. Indeed, the stronger signatures of mortality in this cohort
401 were related to Factors 2 and 3, both characterized by attenuated immune responses.

402

403 A consistent mortality signal in our analyses was related to renal and hepatic dysfunction coupled
404 with impaired fatty acid β -oxidation (Factor 2), strongly associated with the Hyperinflammatory
405 phenotype. Dicarboxylic fatty acids (DCFAs) are generated primarily in liver and kidney through
406 ω -oxidation, an alternative pathway that metabolizes excess fatty acids when mitochondrial β -
407 oxidation is compromised (38, 39). Elevated DCFAs, typically detected in urine of patients with
408 mitochondrial fatty acid oxidation disorders, can further impair mitochondrial respiration and
409 ATP synthesis via mitochondrial uncoupling (40, 41). The combination of elevated DCFAs and
410 low plasmalogen levels also suggests peroxisomal dysfunction, as DCFAs undergo preferential
411 peroxisomal β -oxidation, and peroxisomes are essential for plasmalogen biosynthesis (42, 43).
412 Peroxisomes also play a crucial role in regulating inflammation by maintaining neutrophil
413 membrane phospholipid composition and viability. Together, this metabolic signature, with its
414 persistent elevation over time in non-survivors, implies liver and kidney dysfunction leading to
415 metabolic derangements that could further exacerbate end-organ dysfunction and contribute to
416 impaired immunity, creating a vicious cycle strongly associated with mortality. Therapeutic
417 interventions targeting lipid homeostasis restoration, such as L-carnitine supplementation,
418 plasmalogen replacement, or simvastatin, could be candidates for study in this patient population
419 (43-45).

420

421 Factor 3, strongly associated with both the Hyperinflammatory phenotype and mortality,
422 represents broad impairment in host response with reduced interferon signaling (type I and type
423 II) and lymphoid cell interactions, alongside enrichment of integrated stress response pathways,
424 influenza infection, increased cell turnover, and altered mitochondrial respiration. Suppressed
425 type I interferon responses have been documented in peripheral blood of patients with severe

426 COVID-19, in monocytes from bronchoalveolar lavage of patients with COVID-
427 19/metapneumovirus co-infection, and in pediatric patients with severe respiratory syncytial
428 virus infection (46-48). Similarly, reduced interferon signaling was observed in the MARS1
429 transcriptional phenotype of critically ill sepsis patients at highest mortality risk (49). Whether
430 this broad interferon program suppression results from pathogen-specific mechanisms or host
431 biological heterogeneity remains unclear. Therapeutic interferon- γ has shown promise in sepsis-
432 induced immunosuppression, particularly benefiting patients with decreased monocyte HLA-DR
433 expression and reduced TNF production in response to LPS, and has proven effective in treating
434 fungal sepsis in chronic granulomatous disease and HIV-associated cryptococcal meningitis (50-
435 52).

436

437 Our current findings validate and deepen our previous work on plasma metabolic profiles in
438 ARDS phenotypes (14). While our earlier pilot study identified reduced circulating lipids and
439 elevated glycolytic metabolites in Hyperinflammatory ARDS, our present multi-omic analysis
440 elucidates the mechanistic underpinnings of these derangements. Mitochondrial stress emerged
441 as a central theme across all mortality-associated MEFISTO factors, with lactoyl amino acids—
442 recently established biomarkers of mitochondrial dysfunction in inherited metabolic disorders
443 and predictors of septic shock mortality—significantly elevated in three of the four factors (16,
444 29). Each factor highlighted distinct perturbations in mitochondrial bioenergetics coupled with
445 specific immune signatures: Factor 1 revealed metabolic reprogramming suggestive of the
446 Warburg effect alongside enhanced innate immunity; Factor 2 demonstrated specific deficits in
447 fatty acid β -oxidation with impaired immune responses related to liver dysfunction; Factor 3
448 highlighted increased expression of oxidative phosphorylation and electron transport chain genes

449 coupled with interferon program suppression; and Factor 5 identified mitochondrial redox
450 imbalance with immune cell proliferation and oxidative stress-induced cellular senescence. The
451 metabolic signatures, together with broad depletion of membrane lipids across all factors, offer
452 mechanistic explanations for the reduced circulating lipids previously observed in our work and
453 independent sepsis cohorts (53, 54). This molecular dissection of ARDS heterogeneity
454 demonstrates the intricate interplay between mitochondrial bioenergetics and immunophenotype,
455 suggesting combination therapies targeting both metabolic derangements and inflammation may
456 achieve synergistic reductions in ARDS and sepsis mortality. Notably, previous experimental
457 work identified mitochondrial dysfunction in alveolar epithelial type 2 cells that was rescued by
458 mitochondrial transfer from mesenchymal stromal cells, resulting in recovered surfactant
459 secretion and reduced lung injury severity, highlighting the therapeutic potential of interventions
460 restoring mitochondrial function (55).

461
462 Our phenotype-specific multi-omic analyses reveal that within-phenotype biological
463 heterogeneity had modest associations with mortality. Rather, the primary biological differences
464 driving outcome variation were those that distinguish the inflammatory phenotypes from each
465 other. Nevertheless, examination of mortality-associated signatures within each inflammatory
466 phenotype uncovered distinct mechanistic patterns. In Hypoinflammatory ARDS, the mortality
467 signature was characterized by profound suppression of translation machinery, suppressed
468 adaptive immunity, and enhanced innate immunity. This signature strongly correlated with
469 moderate-to-high dose corticosteroid use within the preceding 24 hours. Since steroid
470 administration in ROSE was clinician-directed rather than protocol-driven, this association may
471 reflect confounding by indication. Without comprehensive data on steroid dosing and duration,

472 this relationship cannot be interpreted as causal. However, existing evidence suggests patients
473 with Hypoinflammatory-like phenotypes may respond poorly to corticosteroids, as demonstrated
474 in a secondary analysis of the VANISH trial, where the Hypoinflammatory phenotype
475 experienced worse outcomes when randomized to corticosteroids (56, 57). These findings
476 suggest that steroid responsiveness may vary significantly among ARDS phenotypes,
477 underscoring the necessity for phenotype-stratified clinical trials to optimize therapeutic
478 approaches.

479

480 In Hyperinflammatory ARDS, mortality was associated with enhanced RUNX1-mediated
481 hematopoietic programs, widespread chromatin remodeling, active cell cycle progression, and
482 oxidative stress-induced senescence. Non-survivors also exhibited HCMV infection pathway
483 enrichment suggesting viral reactivation, and elevation in long chain acyl carnitines and lactoyl
484 amino acids suggestive of mitochondrial metabolic failure. RUNX1 overactivation may be
485 pathogenic, as its knockdown attenuates inflammatory cytokine production in LPS-stimulated
486 macrophages, its inhibition improves survival in septic shock models, and RUNX-1 silencing
487 exosomes ameliorate sepsis-induced AKI in experimental models (58-60).

488

489 Lastly, metabolomic analyses revealed depleted circulating long-chain polyunsaturated fatty
490 acids, likely from oxidative stress-induced peroxidation and consumption of inflammatory lipid
491 mediators, accompanied by elevated plasmalogens and long chain acyl carnitines indicative of
492 impaired fatty acid beta-oxidation. Collectively, these data suggest mortality in the
493 Hyperinflammatory phenotype results from multifactorial dysregulation spanning innate and
494 adaptive immunity, platelet activation, lipid metabolism, and estrogen signaling pathways.

495
496 Our findings offer several clinical implications. The identification of mortality-associated
497 molecular signatures presents opportunities for targeted interventions based on specific
498 biological mechanisms. These signatures remain stable during the initial 48 hours post- ICU
499 admission, providing a potential therapeutic window. Our data indicate multiple contributing
500 pathways to mortality, suggesting combination therapies may yield synergistic benefits, similar
501 to IL-6 inhibitors with dexamethasone in COVID-19 related ARDS (61). Factor 1 represents
502 expansion of immature, immunosuppressive neutrophils characterized by upregulation of
503 emergency granulopoiesis markers (IL1R2, ARG1, CD177, OLFM4), stress response genes
504 (HSPA1A/B, S100A8/9), and tissue-damaging enzymes (MMP8/9), coupled with metabolic
505 hyperactivation (enhanced glycolysis, BCAA metabolism, lipid mediator synthesis), consistent
506 with recent studies showing these populations predict mortality (26). Conversely, Factor 2
507 reflects a metabolically paralyzed state with downregulation of critical antimicrobial peptides
508 (CAMP, DEFA1, LYZ) and defensive molecules (CST3, CFD, BST2) despite slight increases in
509 some granule proteins (MPO, ELANE, PRTN3), alongside disrupted fatty acid metabolism
510 (altered dicarboxylate and monohydroxy fatty acids), impaired protein synthesis responses
511 (EIF2AK4/GCN2), and aberrant GPCR signaling. Genes showing opposing patterns between
512 factors (CYBB, CXCL1, LTF, BPI upregulated in Factor 1, downregulated in Factor 2) suggest
513 Factor 1 cells represent a dysregulated state simultaneously expressing antimicrobial and
514 immunosuppressive markers, while Factor 2 demonstrates clear suppression of antimicrobial
515 competence that may prevent effective pathogen clearance (62). Importantly, Factor 2 accounted
516 for only 1.5% of the explained transcriptomic variance (vs 35% for Factor 1, Table S4),
517 indicating that this transcriptomic signature is a minor contributor to overall outcomes. However,

518 Factor 2 accounted for 46% of explained metabolomic variance, suggesting that fatty acid beta-
519 oxidation impairment likely represents a broader metabolic dysfunction beyond neutrophils
520 alone, potentially affecting multiple cell types and contributing to the systemic metabolic
521 dysregulation observed in severe sepsis and ARDS. With emerging precision medicine platform
522 trials in critical care and point-of-care phenotyping tools for inflammatory phenotypes,
523 therapeutics targeting these signatures can be systematically evaluated across phenotypes (13,
524 63).

525

526 Our study has several key strengths that enhance the robustness and generalizability of its
527 findings. To our knowledge, our analysis, which used samples from 160 patients in the
528 multicenter ROSE trial, represents the largest multi-omics analysis in ARDS to date. Compared
529 to our previous pilot metabolomic investigation, which analyzed a small, selected subset at a
530 single timepoint, the current study employed systematic biospecimen collection with longitudinal
531 sampling and adequate statistical power, detecting substantially greater biological diversity and
532 enabling robust phenotypic comparisons. The clinical trial framework ensured standardized care
533 and systematic biospecimen collection, minimizing treatment-related confounding. Our multi-
534 modal approach provides important insights into cellular programming and systemic metabolism
535 in ARDS and sepsis. The two-timepoint design established signature stability, critical for
536 therapeutic target identification. External validation in EARLI, a diverse sepsis cohort that
537 captures patients early in critical illness, demonstrates these molecular signatures represent
538 generalizable biological states rather than ARDS-specific findings. This cross-syndrome
539 reproducibility strengthens clinical applicability, as therapeutic interventions targeting these
540 signatures could benefit the broader population of critically ill patients with sepsis who share

541 similar molecular phenotypes, aligning with evidence that ARDS inflammatory phenotypes
542 extend to sepsis (24) and overlap with other protein and transcriptional subtypes (49, 57, 64, 65).
543
544 Important limitations include the inability of observational human biospecimen data to establish
545 causality between identified signatures and outcomes. Whole blood transcriptomics precludes
546 attribution of gene expression patterns to specific immune cell populations. While we employed
547 computational deconvolution using CIBERSORTx to estimate cell-type contributions, this
548 approach has inherent limitations including dependence on reference dataset selection, inability
549 to capture disease-specific or novel cell states, and potential confounding by shared gene
550 expression programs across cell types. Nevertheless, deconvolution provided valuable context,
551 revealing that Factor 1's neutrophil degranulation signature correlated strongly with immature
552 progenitor neutrophils, consistent with emergency granulopoiesis rather than functional
553 degranulation by mature neutrophils. Furthermore, transcriptional programs may not reflect
554 functional protein capacity, particularly in contexts such as emergency granulopoiesis where
555 gene expression patterns can be developmentally regulated independently of protein translation.
556 Similarly, untargeted metabolomics provides limited source information for the observed
557 differences in circulation, which may include liver, kidney, and lung. This multi-tissue origin
558 represents both a limitation (we cannot definitively attribute metabolic changes to specific cell
559 types) and a strength (circulating metabolites constitute the metabolic environment shaping
560 immune cell function). The absence of comprehensive pathogen data restricts contextualizing
561 these molecular signatures within the broader pathophysiology of ARDS and sepsis. The
562 pronounced mortality difference between phenotypes in our cohort (24% vs 61%) may have
563 enhanced detection of certain signatures, particularly Factor 5, which explained minimal model

564 variance and may not retain its mortality association in cohorts with smaller phenotype
565 differences. Finally, clinical utility of these molecular signatures requires further investigation in
566 both experimental models and clinical studies.

567

568 In conclusion, this comprehensive multi-omic analysis reveals insights into the molecular
569 heterogeneity of ARDS and sepsis. Inflammatory phenotypes of ARDS and sepsis reflect distinct
570 biological processes with profound differences in mitochondrial function, immune response, and
571 metabolic regulation. Mortality-associated molecular states suggest complex interplay between
572 phenotype-specific and phenotype-independent pathways affecting patient outcomes. Future
573 studies must determine tissue origins of these circulating signatures, the impact of specific
574 pathogens, and test viable therapeutic targets in experimental models, laying groundwork for
575 interventions that address the molecular complexity of critical illness.

576

577

578 **METHODS**

579

580 **Study design and cohorts**

581

582 *Sex as a Biological Variable*

583 Our study examined male and female participants. Sex was included as a covariate in regression
584 analyses.

585

586 *Primary Cohort*

587 The ROSE randomized trial of neuromuscular blockade for moderate-to-severe ARDS enrolled
588 1,006 patients from January 2016 to April 2018 (15). Patients were randomized to continuous
589 cisatracurium infusion with deep sedation versus usual care, with the trial stopping early due to
590 futility for the primary outcome of 90-day mortality. LCA of clinical and protein biomarker data
591 was previously performed on all patients with Day 0 biospecimens available, with participants
592 assigned probabilities of membership to Hyper- or Hypo-inflammatory phenotypes (10). We
593 randomly selected 80 patients from each phenotype who had a >0.9 probability of phenotype
594 membership. This sample size was determined *a priori* to enable detection of differences
595 between survivors and non-survivors within each phenotype, assuming mortality rates of 40% in
596 Hyperinflammatory and 20% in Hypoinflammatory ARDS based on prior studies (5, 6, 8, 9, 11).
597 Using the *MetSizeR* package with probabilistic principle components analysis (PPCA) and a
598 fixed FDR of 0.05, this sample size (32 predicted deaths in Hyperinflammatory and 16 in
599 Hypoinflammatory) provided >90% power to detect metabolic differences via untargeted
600 profiling (27, 66, 67). Samples were obtained from the NHLBI biorepository, BioLINCC.

601
602 *Validation Cohort*
603 The Early Acute Renal and Lung Injury (EARLI) study is an ongoing prospective observational
604 cohort of critically ill adults admitted to ICUs at the University of California San Francisco
605 Moffitt-Long Hospital and Zuckerberg San Francisco General Hospital. Patients are eligible
606 upon ICU admission from the emergency room, excluding those with isolated
607 neurological/neurosurgical indications or trauma service admissions. The University of
608 California San Francisco Institutional Review Board approved this study. From this cohort, we
609 analyzed three partially overlapping subgroups (Supplemental Figure 3): 195 patients with sepsis
610 (2008-2016) who previously underwent metabolic profiling (27); 196 participants with
611 hypotension or requiring invasive mechanical ventilation in the emergency room and sepsis
612 (2010-2018) who previously underwent transcriptomic profiling (28); and 308 patients from 818
613 sepsis patients (2008-2019) who underwent LCA of clinical and protein biomarker data (24).
614 This subset of 308 patients was selected because they had both LCA phenotype designation and
615 either transcriptomic data, metabolomic data, or both available. Sepsis diagnosis was adjudicated
616 through retrospective physician review of electronic medical records using sepsis-2 criteria,
617 incorporating all available clinical and microbiologic data while blinded to phenotype or
618 biological profiling data (68). Patients whose initial sepsis diagnosis occurred >2 days after ICU
619 admission were excluded. We analyzed lactate values from 546 of 818 phenotyped sepsis
620 patients in EARLI who had clinical lactate measurements at days 0-2 of enrollment, including
621 subsequent values for longitudinal comparisons.

622

623 **Biomarker measurements**

624 *Metabolic profiling*

625 EDTA plasma (150 uL) from Day 0 and Day 2 of ROSE trial enrollment was batch shipped to
626 Metabolon (Durham, NC), precipitated with methanol, and underwent untargeted metabolic
627 profiling using three complementary methods: reverse phase chromatography/ultra performance
628 liquid chromatography tandem mass spectrometry (RP/UPLC-MS/MS) with positive
629 electrospray ionization (ESI), RP/UPLC-MS/MS with negative ESI, and hydrophilic interaction
630 liquid chromatography (HILIC)/UPLC-MS/MS with negative ESI. Metabolon performed peak
631 identification using an in-house library in 2023, as well as quality control and batch-
632 normalization.

633

634 In EARLI, 150 uL of citrated plasma underwent identical untargeted profiling methodology, with
635 peaks identified using Metabolon's in-house library in 2017 (27).

636

637 *RNA sequencing*

638 In the ROSE cohort, whole blood samples from Day 0 and Day 2 of trial enrollment were
639 collected in PAXgene tubes, stored at -80°C, and RNA extracted using Qiagen RNEasy kit
640 followed by DNase treatment as previously described (10). In EARLI, whole blood RNA
641 sequencing was performed using a similar methodology (28).

642

643 **Statistical analysis**

644

645 Analyses were conducted in R version 4.3.2. Clinical variables and demographics were
646 compared between the phenotypes using Welch's t-test, Wilcoxon rank-sum test, Chi-squared

647 test, or Fisher's exact test as appropriate based on variable type, distribution, and expected
648 frequency. A p-value less than 0.05 was considered significant.

649
650 For metabolomic analyses, unknown metabolites and those with >25% missingness in both
651 phenotypes were removed. Following Kokla et al.'s approach to minimize imputation error (69),
652 metabolites with >25% missingness in either phenotype were imputed using a uniform
653 distribution ranging from ½ minimum to minimum observed value of the metabolite across all
654 samples. The remaining metabolites were imputed using Random Forest (*missForest*). Metabolic
655 profiles were compared via differential abundance analysis using limma (*MetaboAnalystR*
656 package), adjusting for age, sex, BMI, relevant medications (propofol, dexmedetomidine,
657 corticosteroids), comorbid liver disease, and GFR (70). For Day 2 analyses, randomization arm
658 was added as a covariate, as samples were obtained after the administration of trial agents.
659 Metabolite enrichment analysis was performed using ChemRICH (71), a chemical similarity-
660 based statistical enrichment approach that overcomes limitations of traditional pathway analysis.
661 By grouping metabolites based on chemical ontologies and structural similarity, ChemRICH
662 generates study-specific, non-overlapping metabolite sets with self-contained enrichment
663 statistics independent of background database size. For our analysis, differentially abundant
664 metabolites at each timepoint (Day 0 or Day 2) with their identifiers (SMILES, InChIKeys,
665 PubChem IDs) and Metabolon class annotations. After resolving duplicate entries and
666 completing missing PubChem IDs through database searches, the dataset was processed through
667 the ChemRICH web interface.

668

669 For each metabolite, we constructed linear mixed-effects models to analyze changes in
670 metabolite values over time based on 90-day mortality outcome. The primary model included
671 fixed effects for time, mortality, treatment arm, age, sex, and BMI, with a random intercept for
672 each subject. We tested the significance of the time-by-mortality interaction by comparing this
673 model to a null model without the interaction term using likelihood ratio tests. The coefficient of
674 the time-by-mortality interaction represents the differential trajectory of metabolite levels
675 between survivors and non-survivors from Day 0 to Day 2, with positive values indicating
676 greater increases (or smaller decreases) in non-survivors. P-values from model comparisons
677 (FDR <0.05) were used to assess statistical significance of these differential trajectories. For
678 analysis of metabolic class trajectories over time, we annotated differentially expressed
679 metabolites with pathway information from Metabolon's database. Fold changes were calculated
680 by exponentiating the model coefficients and adding 1, representing the relative change in
681 metabolite levels between survivors and non-survivors. We performed enrichment analysis using
682 ChemRICH as described above. Significantly enriched pathways (FDR<0.05) were classified as
683 increased or decreased based on the proportion (>0.5) of increased metabolites within each
684 pathway.

685

686 For multi-omics analyses in the full study cohort, we implemented a rigorous filtration pipeline
687 to select only the most abundant and variable analytes, thereby avoiding imputation which can
688 introduce artifacts in integrated multi-omics analyses. As such, unknown metabolites and
689 xenobiotics were removed. Metabolites with >10% missingness were removed. Remaining
690 metabolites underwent log transformation, quantile normalization, and selection of the top 500
691 by median absolute deviation (MAD), followed by z-scaling. Transcriptomic data underwent

692 variance stabilizing transformation, with the top 2500 genes selected by MAD and subsequently
693 z-scaled. For each patient, Day 0 and Day 2 metabolite and gene expression data were entered
694 into a MEFISTO model (*mofa2* package) (25). MEFISTO is an unsupervised multi-modal
695 temporally informed dimensionality reduction tool to identify predominant patterns of variation
696 in omics data. MEFISTO extends conventional matrix factorization by incorporating a functional
697 view on latent factors based on Gaussian processes, allowing for modeling of temporal
698 relationships in the data. Our implementation treated the entire patient cohort as a single group
699 while declaring time as a covariate, facilitating joint decomposition of multi-omics data matrices
700 into latent factors (Z) with corresponding feature weights (W), with temporal structure modeled
701 through a squared exponential covariance function. This framework allowed for identification of
702 both smooth (time-dependent) and non-smooth (time-independent) variation patterns, providing
703 insights into temporal dynamics of molecular responses in ARDS patients while accounting for
704 cohort level heterogeneity. After model fitting, the resulting factor values (Z) were extracted to
705 quantify the strength of each identified molecular co-variation pattern for each patient at each
706 timepoint, allowing us to characterize the temporal dynamics of metabolomic and transcriptomic
707 responses in ARDS patients.

708

709 We selected 10 latent factors for initial analysis. The total variance (R^2) explained for each data
710 modality and per factor was calculated to determine the primary sources of dataset heterogeneity.
711 To determine the association of MEFISTO factors with clinical variables, we performed linear
712 regression for categorical predictors (with factor value as the outcome) and Spearman's
713 correlation for continuous predictors using Day 0 factor values. Clinical variables with
714 missingness were left as missing (not imputed). FDR-adjusted p-values <0.05 were considered

715 significant. Gene set enrichment analysis was performed on latent MEFISTO factors using
716 Reactome and MitoCarta 3.0 gene sets, while a metabolite set was generated using Metabolon's
717 annotated library (72, 73). To test for interaction between MEFISTO factors and time regarding
718 mortality, we implemented linear mixed effects regression models with 90-day mortality,
719 timepoint, and their interaction as fixed effects, including a random intercept for each patient to
720 account for within-subject correlation in measurements over time.

721

722 For multi-omics analyses within each LCA phenotype, the same data processing pipeline was
723 applied with MAD-based selection of metabolites and gene transcripts performed within each
724 phenotype.

725

726 To assess the relationship between inferred cell type composition and sample-level factors for
727 Factors 1 and 2, we computed Spearman rank correlations between cell type proportions and
728 factor values across samples. Cell type proportions were estimated using CIBERSORTx,
729 leveraging the reference generated by Kwok et al (26, 74). Spearman correlation coefficients
730 were calculated to identify significant associations between specific cell individual and
731 aggregated populations of interest and factors one and two.

732

733 For validation studies in EARLI, the same pipeline was applied to prepare metabolite and
734 transcriptomic data. The relative weights of the top 100 features within each MEFISTO latent
735 factor that were present in EARLI were used to calculate factor values for each EARLI patient.
736 Specifically, factor values were calculated as the weighted sum of normalized feature

737 measurements, using weights derived from our original MEFISTO model. Associations between
738 factor values per patient and clinical outcomes were tested using Wilcoxon rank sum tests.

739

740 All analyses were adjusted for multiple comparisons using the Benjamini-Hochberg false
741 discovery rate (FDR) with significance set at $FDR < 0.05$.

742

743 **Study Approval**

744 The Institutional Review Board of the University of California, San Francisco approved the
745 enrollment of human subjects in the EARLI observational cohort and the ROSE randomized
746 controlled trial.

747

748 **Data Availability**

749 Supporting values for all the manuscript and supplemental figures, including complete results of
750 gene and metabolite set enrichment analyses, are provided in the Supporting Data Values

751 supplemental file. Transcriptomic data for the ROSE trial participants is available at

752 https://www.ncbi.nlm.nih.gov/projects/gap/cgi-bin/study.cgi?study_id=phs003929.v1.p1.

753 Metabolomic data have been deposited in the NIH Metabolomics Workbench (uploaded October

754 16 2025, DOI: <http://dx.doi.org/10.21228/M8ZV9M>) (75). Clinical data and biospecimens from

755 the ROSE trial are available through the NHLBI BioLINCC repository

756 (<https://biolincc.nhlbi.nih.gov/studies/>) to qualified researchers upon request and completion of

757 appropriate data use agreements. The code for the analyses performed in this manuscript is

758 available on https://git.ucsf.edu/narges-alipanah/rose_manuscript/.

759

760 **Author contributions**

761 NA, LN, and CSC contributed to the conceptualization of this work. NA, LN, AS, and CSC
762 developed the methodology. NA and LN conducted the investigation and created the
763 visualizations. NA and CSC acquired funding for the project. Project administration was
764 performed by NA, LN, CLe, KB, SC, OC, SH, TH, CH, KK, CRL, DL, CLi, KL, LM, AR, AS,
765 EM, NS, KAS, MW, AW, HZ, MAM, and CSC. NA and CSC provided supervision. NA, LN, and
766 CSC wrote the original draft. NA, LN, PS, CLe, KB, SC, OC, SH, TH, CH, KK, CRL, DL, CLi,
767 KL, LM, AR, AS, ES, NS, KS, MW, AW, HZ, AJR, KAS, MAM, and CSC reviewed and edited
768 the manuscript.

769

770 NA and LN are co-first authors. The order of names was determined based on Narges Alipanah-
771 Lechner driving the study concept, conducting the metabolomics analyses, and contributing to
772 the biological interpretation, while Lucile Neyton led the transcriptomic analyses and designed
773 the computational approach. Both authors made substantial and essential contributions to the
774 work.

775

776 **Acknowledgments**

777 We gratefully acknowledge the ROSE trial investigators, the Prevention and Early Treatment of
778 Acute Lung Injury (PETAL) Network, and the National Heart, Lung, and Blood Institute
779 (NHLBI) Biologic Specimen and Data Repository Information Coordinating Center (BioLINCC)
780 for providing the data and biospecimens that made this research possible.

781 We also gratefully acknowledge the participants and participants' families in both the ROSE and
782 EARLI studies.

783

784

785 **References**

- 786 1. Bellani G, et al. Epidemiology, Patterns of Care, and Mortality for Patients With Acute
787 Respiratory Distress Syndrome in Intensive Care Units in 50 Countries. *JAMA*.
788 2016;315(8):788-800.
- 789 2. Rudd KE, et al. Global, regional, and national sepsis incidence and mortality, 1990-2017:
790 analysis for the Global Burden of Disease Study. *Lancet*. 2020;395(10219):200-11.
- 791 3. Marshall JC. Why have clinical trials in sepsis failed? *Trends Mol Med*. 2014;20(4):195-
792 203.
- 793 4. Matthay MA, et al. Clinical trials in acute respiratory distress syndrome: challenges and
794 opportunities. *Lancet Respir Med*. 2017;5(6):524-34.
- 795 5. Calfee C, et al. Subphenotypes in acute respiratory distress syndrome: latent class
796 analysis of data from two randomised controlled trials. *The Lancet Respiratory medicine*.
797 2014;2(8).
- 798 6. Calfee C, et al. Acute respiratory distress syndrome subphenotypes and differential
799 response to simvastatin: secondary analysis of a randomised controlled trial. *The Lancet*
800 *Respiratory medicine*. 2018;6(9).
- 801 7. Sinha P, et al. Prevalence of phenotypes of acute respiratory distress syndrome in
802 critically ill patients with COVID-19: a prospective observational study. *Lancet Respir*
803 *Med*. 2020;8(12):1209-18.
- 804 8. Sinha P, et al. Latent class analysis-derived subphenotypes are generalisable to
805 observational cohorts of acute respiratory distress syndrome: a prospective study. 2021.

- 806 9. Sinha P, et al. Latent class analysis of ARDS subphenotypes: a secondary analysis of the
807 statins for acutely injured lungs from sepsis (SAILS) study. *Intensive Care Med.*
808 2018;44(11):1859-69.
- 809 10. Sinha P, et al. Molecular Phenotypes of Acute Respiratory Distress Syndrome in the
810 ROSE Trial Have Differential Outcomes and Gene Expression Patterns That Differ at
811 Baseline and Longitudinally over Time. *Am J Respir Crit Care Med.* 2024;209(7):816-28.
- 812 11. Famous K, et al. Acute Respiratory Distress Syndrome Subphenotypes Respond
813 Differently to Randomized Fluid Management Strategy. *American journal of respiratory*
814 *and critical care medicine.* 2017;195(3).
- 815 12. Delucchi K, et al. Stability of ARDS subphenotypes over time in two randomised
816 controlled trials. *Thorax.* 2018;73(5):439-45.
- 817 13. Practical PTI, and investigators R-C. The Rise of Adaptive Platform Trials in Critical
818 Care. *Am J Respir Crit Care Med.* 2024;209(5):491-6.
- 819 14. Alipanah-Lechner N, et al. Plasma metabolic profiling implicates dysregulated lipid
820 metabolism and glycolytic shift in hyperinflammatory ARDS. *Am J Physiol Lung Cell*
821 *Mol Physiol.* 2023;324(3):L297-L306.
- 822 15. Moss M, et al. Early Neuromuscular Blockade in the Acute Respiratory Distress
823 Syndrome. Reply. *N Engl J Med.* 2019;381(8):787-8.
- 824 16. Sharma R, et al. Circulating markers of NADH-reductive stress correlate with
825 mitochondrial disease severity. *J Clin Invest.* 2021;131(2).
- 826 17. Levy B. Bench-to-bedside review: Is there a place for epinephrine in septic shock? *Crit*
827 *Care.* 2005;9(6):561-5.

- 828 18. Day NP, et al. The effects of dopamine and adrenaline infusions on acid-base balance and
829 systemic haemodynamics in severe infection. *Lancet*. 1996;348(9022):219-23.
- 830 19. Suomalainen A, et al. FGF-21 as a biomarker for muscle-manifesting mitochondrial
831 respiratory chain deficiencies: a diagnostic study. *Lancet Neurol*. 2011;10(9):806-18.
- 832 20. Debray FG, et al. Diagnostic accuracy of blood lactate-to-pyruvate molar ratio in the
833 differential diagnosis of congenital lactic acidosis. *Clin Chem*. 2007;53(5):916-21.
- 834 21. Kemperman RH, et al. B-169 Beta-hydroxybutyrate/acetoacetate Ratio as Indicator for
835 Mitochondrial Diseases Utilizing a Novel LC-MS/MS Based Ketone Body Panel.
836 *Clinical Chemistry*. 2023;69(Supplement_1).
- 837 22. Martinez-Reyes I, and Chandel NS. Mitochondrial TCA cycle metabolites control
838 physiology and disease. *Nat Commun*. 2020;11(1):102.
- 839 23. Li X, et al. Lactate metabolism in human health and disease. *Signal Transduct Target*
840 *Ther*. 2022;7(1):305.
- 841 24. Sinha P, et al. Identifying molecular phenotypes in sepsis: an analysis of two prospective
842 observational cohorts and secondary analysis of two randomised controlled trials. *Lancet*
843 *Respir Med*. 2023;11(11):965-74.
- 844 25. Velten B, et al. Identifying temporal and spatial patterns of variation from multimodal
845 data using MEFISTO. *Nat Methods*. 2022;19(2):179-86.
- 846 26. Kwok AJ, et al. Neutrophils and emergency granulopoiesis drive immune suppression
847 and an extreme response endotype during sepsis. *Nat Immunol*. 2023;24(5):767-79.
- 848 27. Rogers AJ, et al. Plasma Metabolites in Early Sepsis Identify Distinct Clusters Defined
849 by Plasma Lipids. *Crit Care Explor*. 2021;3(8):e0478.

- 850 28. Kalantar KL, et al. Integrated host-microbe plasma metagenomics for sepsis diagnosis in
851 a prospective cohort of critically ill adults. *Nat Microbiol.* 2022;7(11):1805-16.
- 852 29. Rogers RS, et al. Circulating N-lactoyl-amino acids and N-formyl-methionine reflect
853 mitochondrial dysfunction and predict mortality in septic shock. *Metabolomics.*
854 2024;20(2):36.
- 855 30. Ahl PJ, et al. Met-Flow, a strategy for single-cell metabolic analysis highlights dynamic
856 changes in immune subpopulations. *Commun Biol.* 2020;3(1):305.
- 857 31. Stienstra R, et al. Specific and Complex Reprogramming of Cellular Metabolism in
858 Myeloid Cells during Innate Immune Responses. *Cell Metab.* 2017;26(1):142-56.
- 859 32. Davies LC, et al. Diversity and environmental adaptation of phagocytic cell metabolism.
860 *J Leukoc Biol.* 2019;105(1):37-48.
- 861 33. Raghuraman S, et al. The Emerging Role of Epigenetics in Inflammation and
862 Immunometabolism. *Trends Endocrinol Metab.* 2016;27(11):782-95.
- 863 34. Ratter JM, et al. Environmental Signals Influencing Myeloid Cell Metabolism and
864 Function in Diabetes. *Trends Endocrinol Metab.* 2018;29(7):468-80.
- 865 35. Gaber T, et al. Metabolic regulation of inflammation. *Nat Rev Rheumatol.*
866 2017;13(5):267-79.
- 867 36. Marelli-Berg FM, and Jangani M. Metabolic regulation of leukocyte motility and
868 migration. *J Leukoc Biol.* 2018;104(2):285-93.
- 869 37. Ratter JM, et al. In vitro and in vivo Effects of Lactate on Metabolism and Cytokine
870 Production of Human Primary PBMCs and Monocytes. *Front Immunol.* 2018;9:2564.
- 871 38. Christensen E, et al. Omega-oxidation of fatty acids studied in isolated liver cells.
872 *Biochim Biophys Acta.* 1991;1081(2):167-73.

- 873 39. Goetzman ES, et al. Dietary dicarboxylic acids provide a non-storable alternative fat
874 source that protects mice against obesity. *J Clin Invest.* 2024;134(12).
- 875 40. Kumps A, et al. Metabolic, nutritional, iatrogenic, and artifactual sources of urinary
876 organic acids: a comprehensive table. *Clin Chem.* 2002;48(5):708-17.
- 877 41. Tonsgard JH, and Getz GS. Effect of Reye's syndrome serum on isolated chinchilla liver
878 mitochondria. *J Clin Invest.* 1985;76(2):816-25.
- 879 42. Ranea-Robles P, and Houten SM. The biochemistry and physiology of long-chain
880 dicarboxylic acid metabolism. *Biochem J.* 2023;480(9):607-27.
- 881 43. Bozelli JC, Jr., et al. Plasmalogens and Chronic Inflammatory Diseases. *Front Physiol.*
882 2021;12:730829.
- 883 44. Morel J, et al. Simvastatin pre-treatment improves survival and mitochondrial function in
884 a 3-day fluid-resuscitated rat model of sepsis. *Clin Sci (Lond).* 2017;131(8):747-58.
- 885 45. Jones AE, et al. Effect of Levocarnitine vs Placebo as an Adjunctive Treatment for Septic
886 Shock: The Rapid Administration of Carnitine in Sepsis (RACE) Randomized Clinical
887 Trial. *JAMA Netw Open.* 2018;1(8):e186076.
- 888 46. Hadjadj J, et al. Impaired type I interferon activity and inflammatory responses in severe
889 COVID-19 patients. *Science.* 2020;369(6504):718-24.
- 890 47. Heinonen S, et al. Immune profiles provide insights into respiratory syncytial virus
891 disease severity in young children. *Sci Transl Med.* 2020;12(540).
- 892 48. Bost P, et al. Host-Viral Infection Maps Reveal Signatures of Severe COVID-19 Patients.
893 *Cell.* 2020;181(7):1475-88 e12.
- 894 49. Scicluna BP, et al. Classification of patients with sepsis according to blood genomic
895 endotype: a prospective cohort study. *Lancet Respir Med.* 2017;5(10):816-26.

- 896 50. Docke WD, et al. Monocyte deactivation in septic patients: restoration by IFN-gamma
897 treatment. *Nat Med.* 1997;3(6):678-81.
- 898 51. Marciano BE, et al. Long-term interferon-gamma therapy for patients with chronic
899 granulomatous disease. *Clin Infect Dis.* 2004;39(5):692-9.
- 900 52. Jarvis JN, et al. Adjunctive interferon-gamma immunotherapy for the treatment of HIV-
901 associated cryptococcal meningitis: a randomized controlled trial. *AIDS.*
902 2012;26(9):1105-13.
- 903 53. Chouchane O, et al. The Plasma Lipidomic Landscape in Patients with Sepsis due to
904 Community-acquired Pneumonia. *Am J Respir Crit Care Med.* 2024;209(8):973-86.
- 905 54. McCann MR, et al. Early Sepsis Metabolic Changes in Kidney and Liver Precede
906 Clinical Evidence of Organ Dysfunction. *Am J Respir Cell Mol Biol.* 2025.
- 907 55. Islam MN, et al. Mitochondrial transfer from bone-marrow-derived stromal cells to
908 pulmonary alveoli protects against acute lung injury. *Nat Med.* 2012;18(5):759-65.
- 909 56. Antcliffe DB, et al. Transcriptomic Signatures in Sepsis and a Differential Response to
910 Steroids. From the VANISH Randomized Trial. *Am J Respir Crit Care Med.*
911 2019;199(8):980-6.
- 912 57. Neyton LPA, et al. Host and Microbe Blood Metagenomics Reveals Key Pathways
913 Characterizing Critical Illness Phenotypes. *Am J Respir Crit Care Med.* 2024;209(7):805-
914 15.
- 915 58. Cunningham L, et al. Identification of benzodiazepine Ro5-3335 as an inhibitor of CBF
916 leukemia through quantitative high throughput screen against RUNX1-CBFbeta
917 interaction. *Proc Natl Acad Sci U S A.* 2012;109(36):14592-7.

- 918 59. Luo MC, et al. Runt-related Transcription Factor 1 (RUNX1) Binds to p50 in
919 Macrophages and Enhances TLR4-triggered Inflammation and Septic Shock. *J Biol*
920 *Chem.* 2016;291(42):22011-20.
- 921 60. Zhang Y, et al. Endothelial progenitor cells-derived exosomal microRNA-21-5p alleviates
922 sepsis-induced acute kidney injury by inhibiting RUNX1 expression. *Cell Death Dis.*
923 2021;12(4):335.
- 924 61. Zeraatkar D, et al. Use of tocilizumab and sarilumab alone or in combination with
925 corticosteroids for covid-19: systematic review and network meta-analysis. *BMJ Med.*
926 2022;1(1):e000036.
- 927 62. Pham L, et al. Neutrophil trafficking to the site of infection requires Cpt1a-dependent
928 fatty acid beta-oxidation. *Commun Biol.* 2022;5(1):1366.
- 929 63. McAuley D. Clinical Evaluation of a Point of Care (POC) Assay to Identify Phenotypes
930 in the Acute Respiratory Distress Syndrome (PHIND).
931 <https://clinicaltrials.gov/study/NCT04009330>. Accessed 02/20/2025.
- 932 64. Bos LDJ, et al. Understanding Heterogeneity in Biologic Phenotypes of Acute
933 Respiratory Distress Syndrome by Leukocyte Expression Profiles. *Am J Respir Crit Care*
934 *Med.* 2019;200(1):42-50.
- 935 65. Davenport EE, et al. Genomic landscape of the individual host response and outcomes in
936 sepsis: a prospective cohort study. *Lancet Respir Med.* 2016;4(4):259-71.
- 937 66. Finucane K, et al. In: Finucane K ed.; 2021.
- 938 67. Nyamundanda G, et al. MetSizeR: selecting the optimal sample size for metabolomic
939 studies using an analysis based approach. *BMC Bioinformatics.* 2013;14:338.

940 68. Levy MM, et al. 2001 SCCM/ESICM/ACCP/ATS/SIS International Sepsis Definitions
941 Conference. *Crit Care Med.* 2003;31(4):1250-6.

942 69. Kokla M, et al. Random forest-based imputation outperforms other methods for imputing
943 LC-MS metabolomics data: a comparative study. *BMC Bioinformatics.* 2019;20(1):492.

944 70. Pang Z, et al. MetaboAnalystR 4.0: a unified LC-MS workflow for global metabolomics.
945 *Nat Commun.* 2024;15(1):3675.

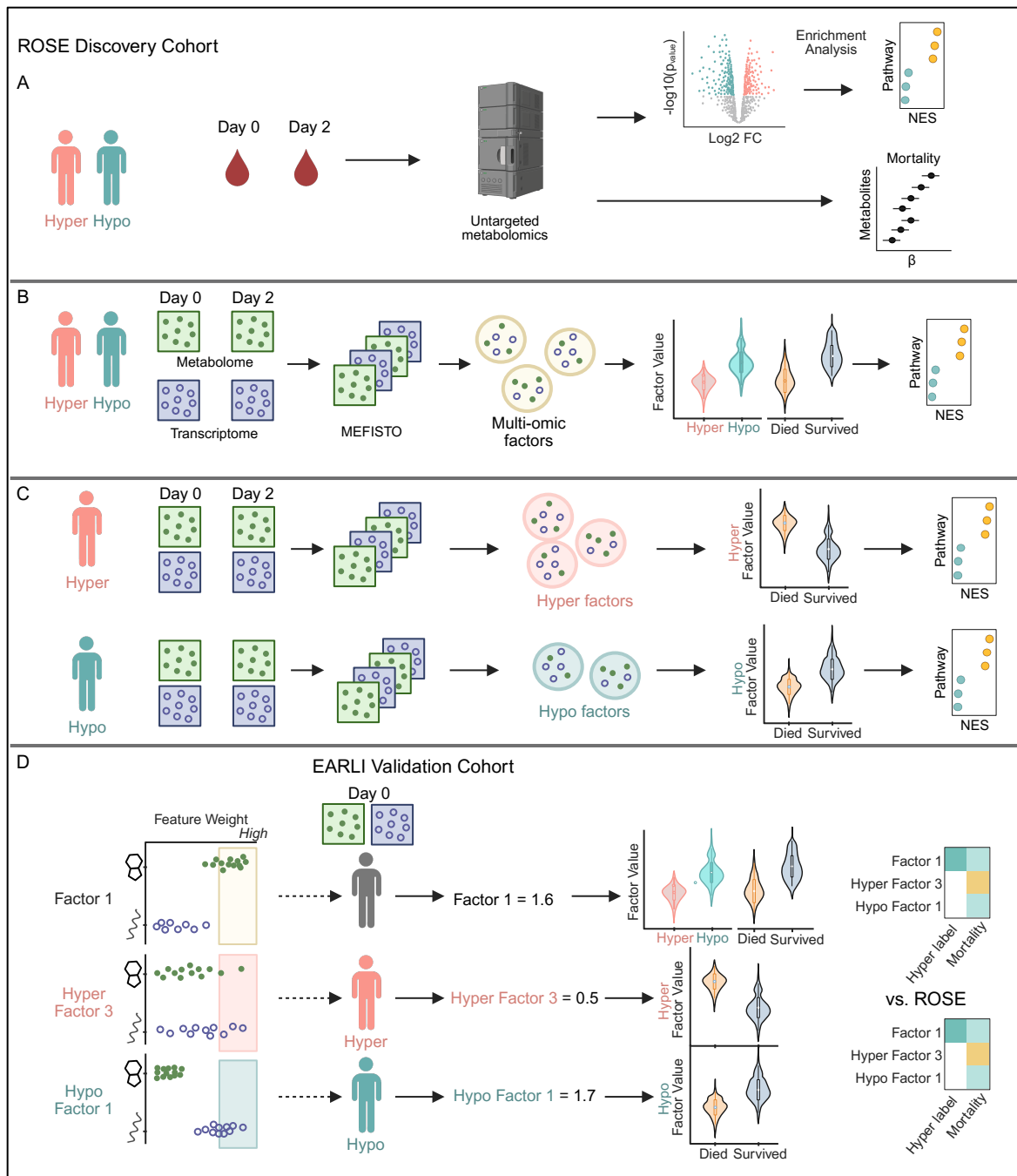
946 71. Barupal DK, and Fiehn O. Chemical Similarity Enrichment Analysis (ChemRICH) as
947 alternative to biochemical pathway mapping for metabolomic datasets. *Sci Rep.*
948 2017;7(1):14567.

949 72. Rath S, et al. MitoCarta3.0: an updated mitochondrial proteome now with sub-organelle
950 localization and pathway annotations. *Nucleic Acids Res.* 2021;49(D1):D1541-D7.

951 73. Milacic M, et al. The Reactome Pathway Knowledgebase 2024. *Nucleic Acids Res.*
952 2024;52(D1):D672-D8.

953 74. Newman AM, et al. Determining cell type abundance and expression from bulk tissues
954 with digital cytometry. *Nat Biotechnol.* 2019;37(7):773-82.

955 75. Sud M, et al. Metabolomics Workbench: An international repository for metabolomics
956 data and metadata, metabolite standards, protocols, tutorials and training, and analysis
957 tools. *Nucleic Acids Res.* 2016;44(D1):D463-70.
958
959

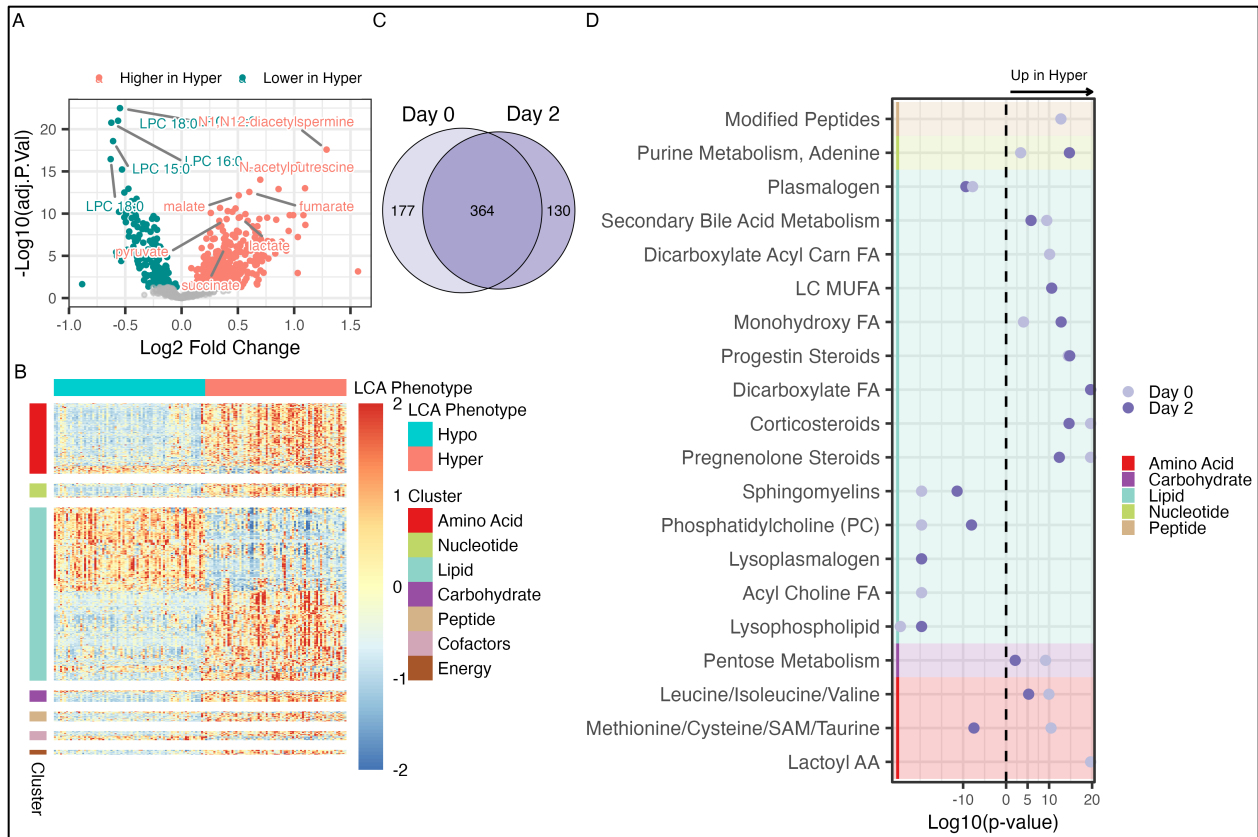


960

961 **Figure 1. Study overview.** (A) Day 0 and Day 2 EDTA plasma from ROSE study participants
 962 underwent untargeted metabolic profiling to determine differences between latent class analysis
 963 (LCA) based inflammatory phenotypes. (B) Longitudinal whole blood transcriptomic data and
 964 metabolomic data were analyzed using an unsupervised multi-modal factor analysis (MEFISTO)
 965 and the predominant sources of biological heterogeneity in the data of clinical relevance were

966 assessed. (C) MEFISTO was applied separately to each phenotype to determine signatures
967 related to mortality within each phenotype. (D) The highest weighted features (metabolite or
968 gene) by absolute value within each multi-omic factor of interest were used to calculate factor
969 weights for patients in an observational cohort study (EARLI). The association of factor weights
970 with LCA phenotypes and outcomes in the validation cohort was assessed. NES = normalized
971 enrichment score. Created in BioRender.

972

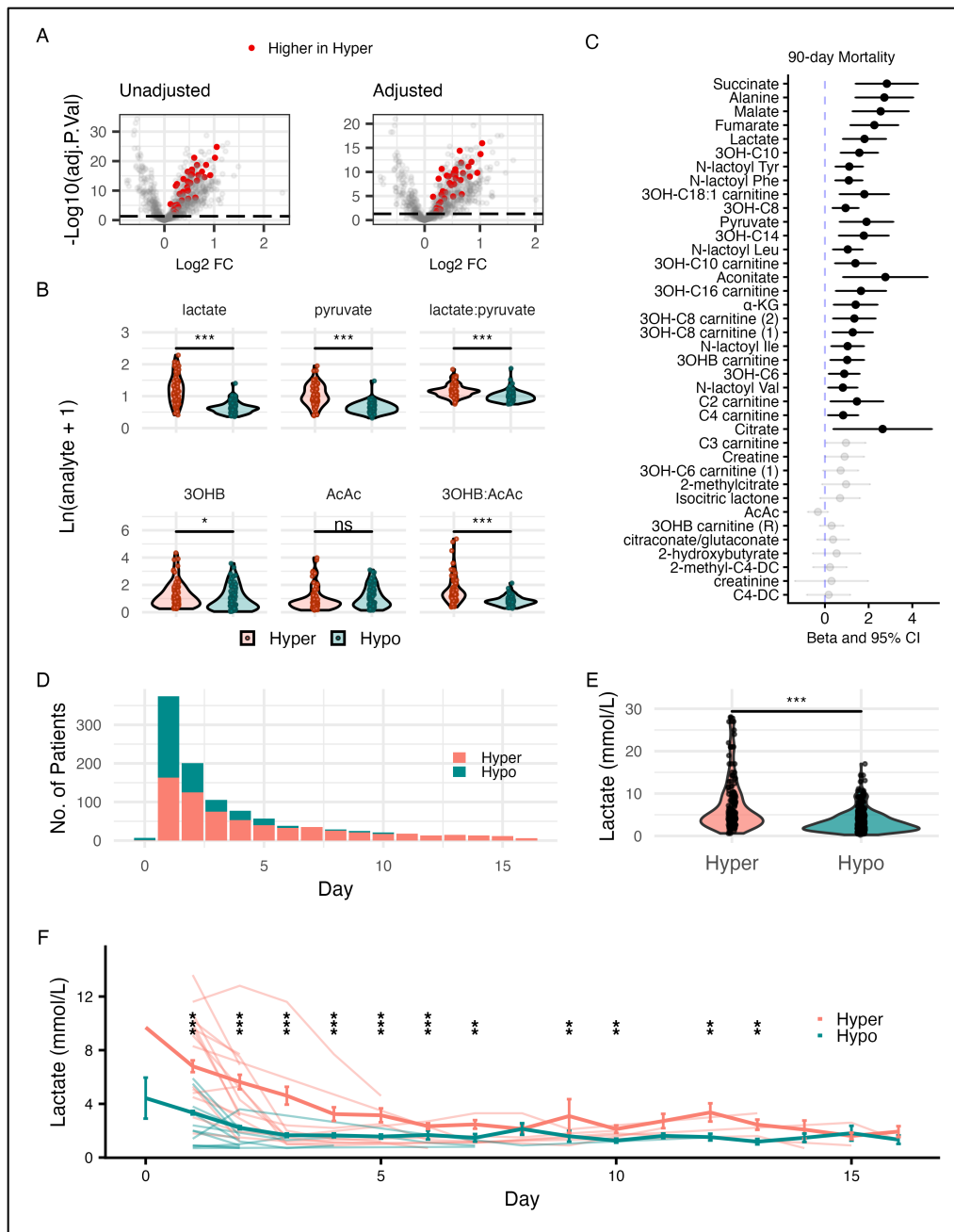


973

974 **Figure 2. Metabolic profiling of latent class analysis (LCA) phenotypes (N = 160 patients).**

975 (A) Volcano plot showing differentially abundant metabolites between Hyperinflammatory and
 976 Hypoinflammatory ARDS at Day 0, determined by limma adjusted for covariates (age, sex, BMI,
 977 medications, liver disease, and GFR). (B) Heatmap of differentially abundant metabolites by
 978 LCA phenotype at Day 0 as determined by limma with adjustment for aforementioned
 979 covariates. Z-scaled log-transformed metabolite intensities are grouped by phenotype. (C) Venn
 980 diagram showing overlap of differentially abundant metabolites at Day 0 and Day 2 (Day 2 also
 981 adjusted for randomization arm). (D) Metabolite pathway enrichment analysis comparing
 982 Hyperinflammatory vs Hypoinflammatory groups at Day 0 and Day 2. X-axis shows signed
 983 log₁₀(p-value), with positive values indicating positive enrichment in Hyperinflammatory group
 984 and negative values indicating positive enrichment in Hypoinflammatory group. Top 20

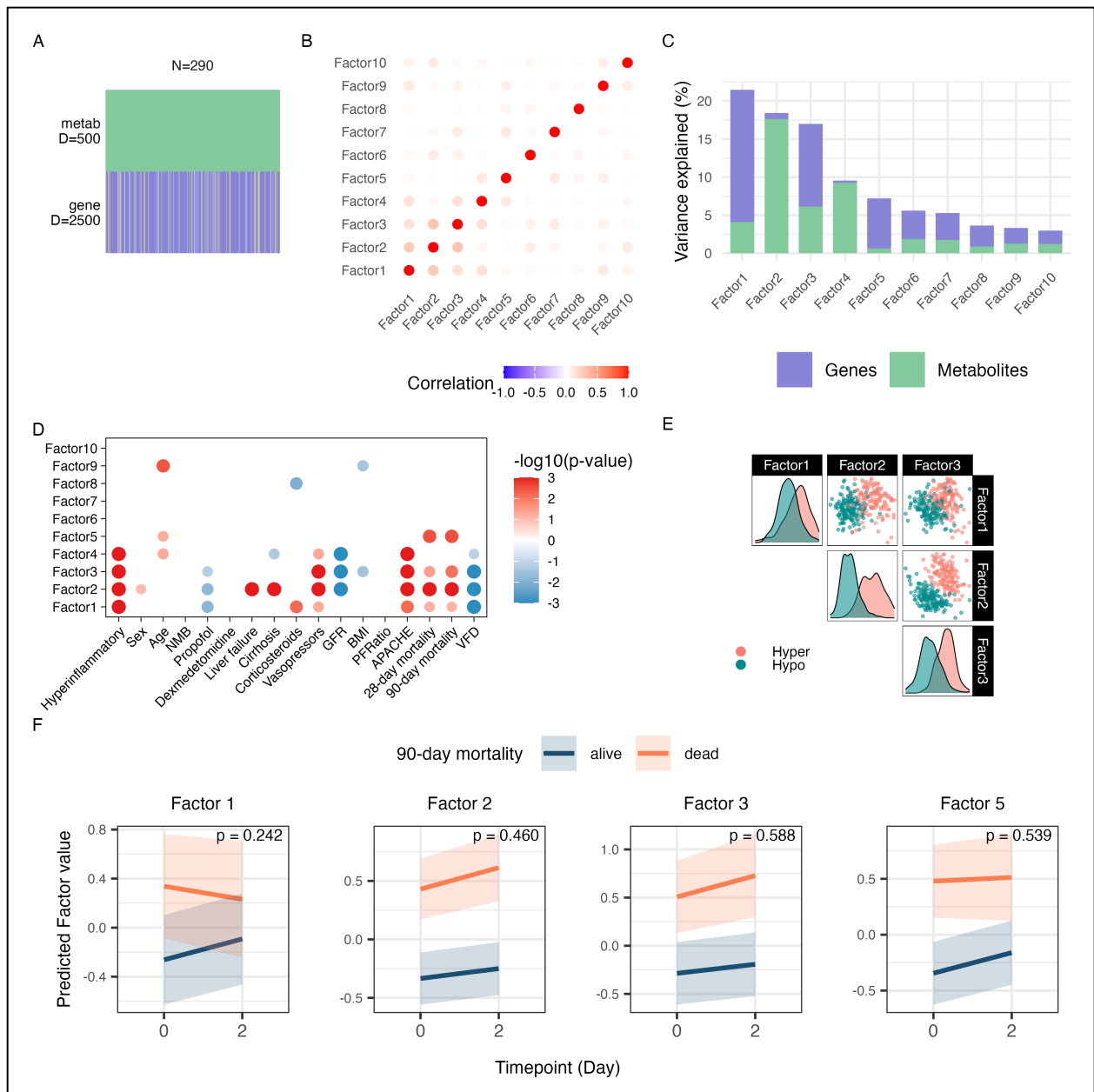
985 significant pathways are shown. AA = amino acid; Carn = carnitine; FA = fatty acid; LC = long
986 chain; MUFA = monounsaturated fatty acid; SAM = S-adenosylmethionine.
987



988

989 **Figure 3. Mitochondrial metabolic derangements across LCA phenotypes.** (A) Volcano plots
 990 comparing hyperinflammatory vs. hypoinflammatory phenotypes at Day 0 in ROSE (N = 160.
 991 Patients). Left: Unadjusted analysis showing statistical significance (limma) vs log2 fold-change.
 992 Right: Analysis adjusted for age, sex, BMI, and vasopressor use. Solid colors represent
 993 mitochondrial metabolites. (B) Peak intensities of redox-coupled mitochondrial metabolites at

994 Day 0 in ROSE (N = 160 patients). (C) Association of mitochondrial metabolites at Day 0 with
995 90-day mortality in ROSE patients (N = 160). X-axis depicts regression coefficients with 95%
996 confidence intervals from logistic regression models using log-transformed peak intensity as the
997 primary predictor, adjusted for age, sex, BMI, and vasopressor use. Solid circles represent FDR
998 p-value <0.05. (D) Distribution of patients with clinical lactate measurements by LCA phenotype
999 and enrollment day in the EARLI cohort (N= 546, Hypoinflammatory: 380, Hyperinflammatory:
1000 166). (E) Comparison of highest clinical lactate value (days 0-2 post-enrollment) per patient by
1001 phenotype in EARLI. (F) Longitudinal clinical lactate trajectories by phenotype showing mean ±
1002 standard error. Individual patient trajectories (random sample) are depicted, excluding those with
1003 lactate value >15 mmol/L for visualization clarity. Wilcoxon rank-sum test p-values <0.05 shown
1004 for each timepoint. * p<0.05, ** p<0.01, *** p<0.001. 3OHB: 3-hydroxybutyrate; FC: fold-
1005 change
1006



1007

1008 **Figure 4. Multi-omics factor analysis (MEFISTO) overview and association with clinical**

1009 **outcomes. (A)** MEFISTO model overview with 290 samples (from 160 patients across two

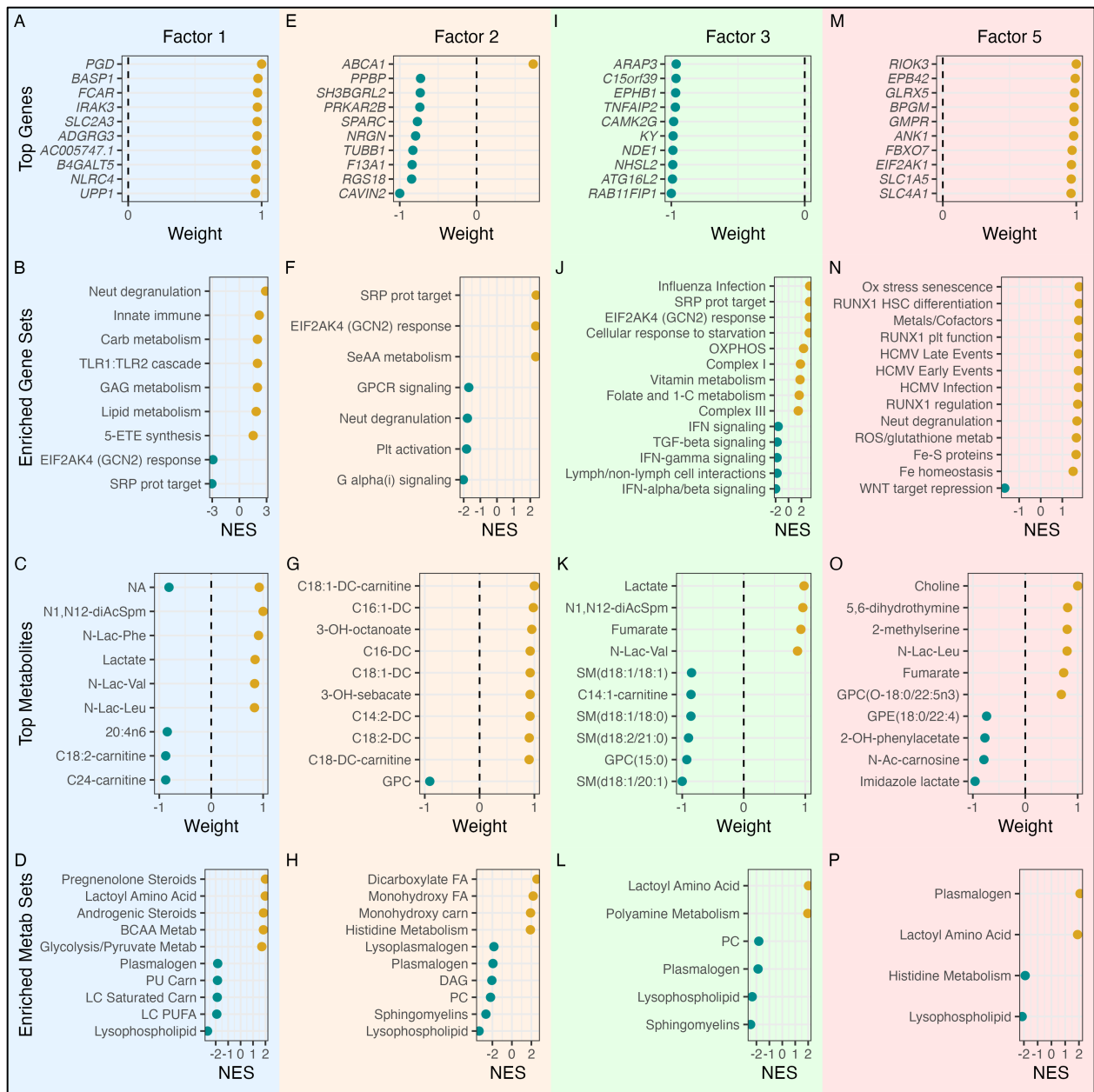
1010 timepoints), top 500 metabolites and top 2500 gene transcripts by median absolute deviation. **(B)**

1011 Spearman's correlation plot of 10 MEFISTO factors based on factor values. **(C)** Proportion of

1012 total variance explained by each factor and each data modality (metabolite vs gene transcript).

1013 **(D)** The association of MEFISTO factor values at Day 0 with clinical variables. Size and

1014 transparency of the dots represent strength of association as determined via Spearman's
1015 correlation for continuous predictors or linear regression for categorical predictors (FDR <0.05).
1016 Color represents directionality of the correlation. (E) Paired plots of MEFISTO factor values per
1017 patient sample, colored by LCA phenotype designation. (F) The slope of change in factor values
1018 over time by survival. Only factors associated with mortality at Day 0 are depicted. P-value
1019 derived from interaction term of a linear mixed effects regression model with 90-day mortality,
1020 timepoint and their interaction as fixed effects and patient as random effect. APACHE = Acute
1021 Physiology and Chronic Health Evaluation III score; BMI = body mass index; GFR = glomerular
1022 filtration rate; metab = metabolite; NMB = neuromuscular blockade; PFRatio = PaO₂:FiO₂ at
1023 the time of enrollment in the ROSE trial; VFD = ventilator free days
1024



1025

1026 **Figure 5. Top features and pathways within mortality-associated MEFISTO Factors. (A, E,**

1027 **I, M) Top 10 genes by relative scaled weight in each factor. (B, F, J, N) Select top gene set**

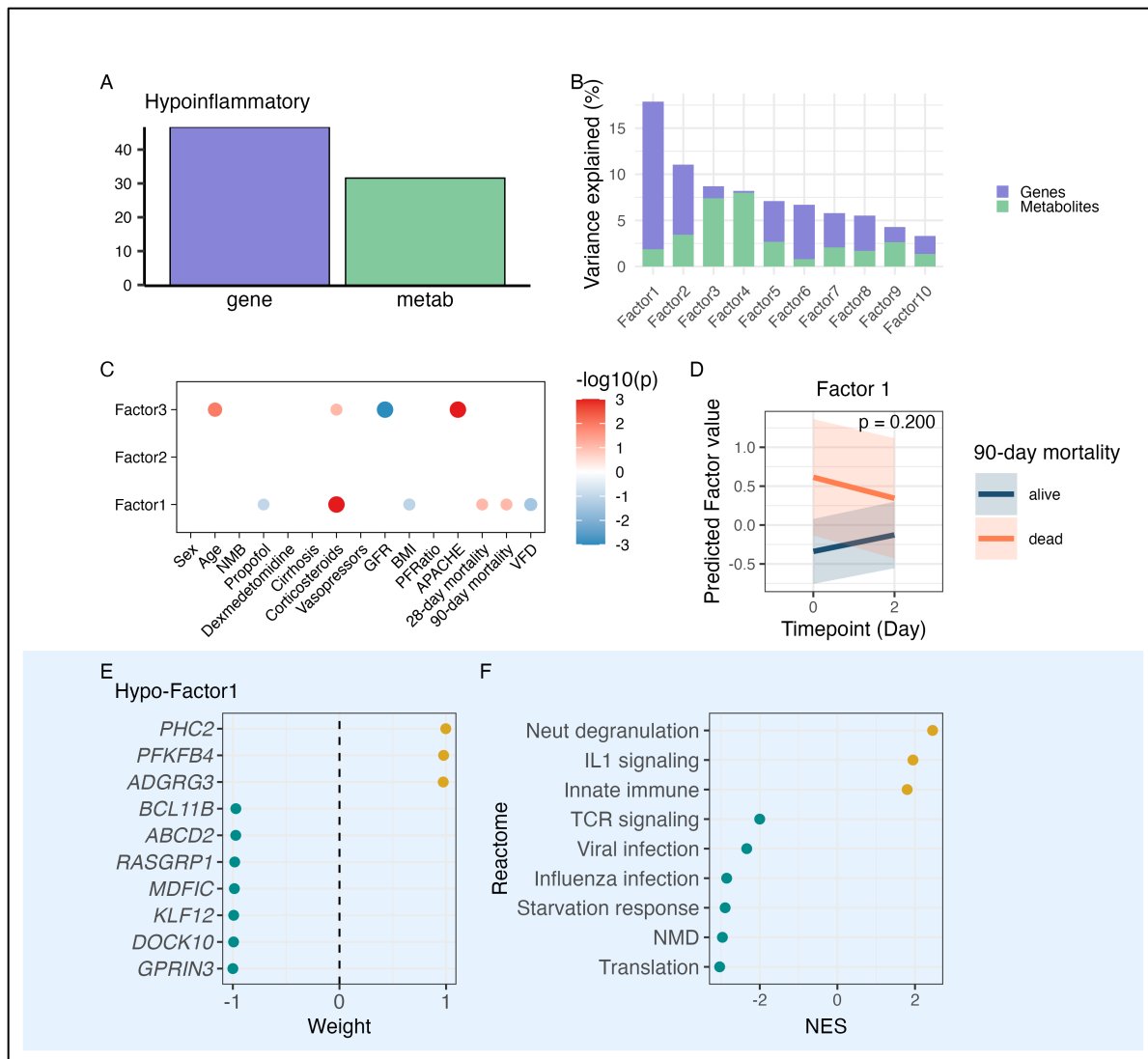
1028 **enrichment pathways in each factor using Reactome unless otherwise stated. X-axis depicts**

1029 **normalized enrichment score (NES). (C, G, K, O) Top 10 metabolites by relative scaled weight**

1030 **in each factor. (D, H, L, P) Top metabolic pathways. X-axis depicts normalized enrichment score**

1031 **(NES). 5-ETE = 5-eicosatetraenoic acids; BCAA = branched chain amino acid; Carb =**

1032 carbohydrate; carn = carnitine; DAG = diacylglycerols; FA = fatty acid; GAG =
1033 glycosaminoglycan; GPCR = G protein-coupled receptor; HSC = hematopoietic stem cell; IFN =
1034 interferon; LC = long chain; Metab = metabolism; Neut = neutrophil; plt = platelet; Ox =
1035 oxidative; OXPHOS = oxidative phosphorylation; PUFA = polyunsaturated fatty acid; SeAA =
1036 selenoamino acid; ROS = reactive oxygen species; SRP = signal recognition particle; TLR = toll
1037 like receptor
1038



1039

1040 **Figure 6. Hypoinflammatory MEFISTO and mortality-associated signature.** Analysis of 153

1041 samples from 80 patients at two timepoints. **(A)** Proportion of total variance explained per

1042 MEFISTO factor and per data modality (gene, metabolite). **(B)** Proportion of total variance

1043 explained per MEFISTO factor. **(C)** Association of MEFISTO factors with clinical variables at

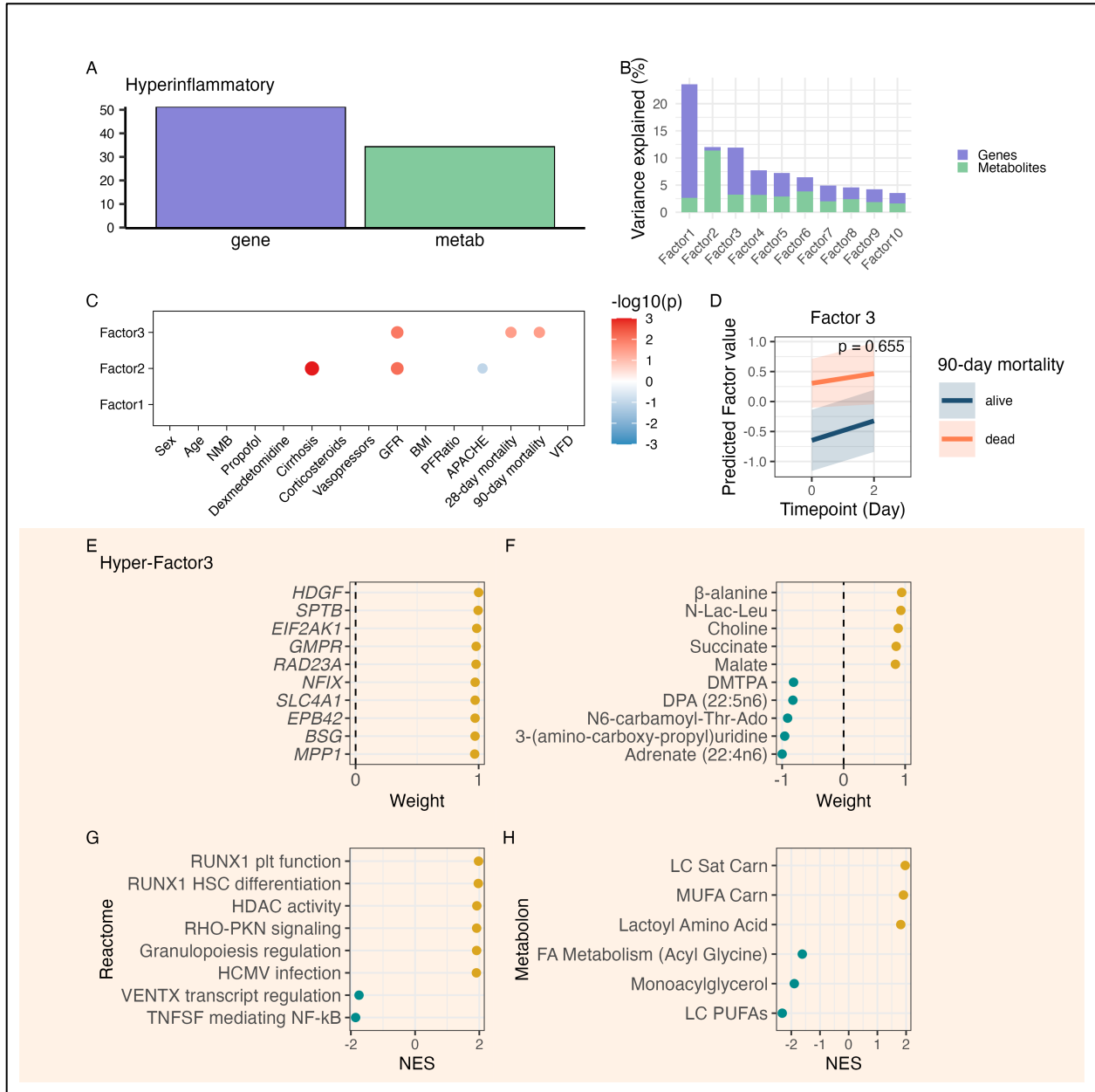
1044 Day 0 as determined via Spearman's correlation for continuous predictors and linear regression

1045 for categorical predictors (FDR <0.05). **(D)** The slope of change in factor 1 over time by 90-day

1046 mortality. P-value derived from interaction term of a linear mixed effects regression model with

1047 90-day mortality, timepoint and their interaction as fixed effects and patient as random effect.

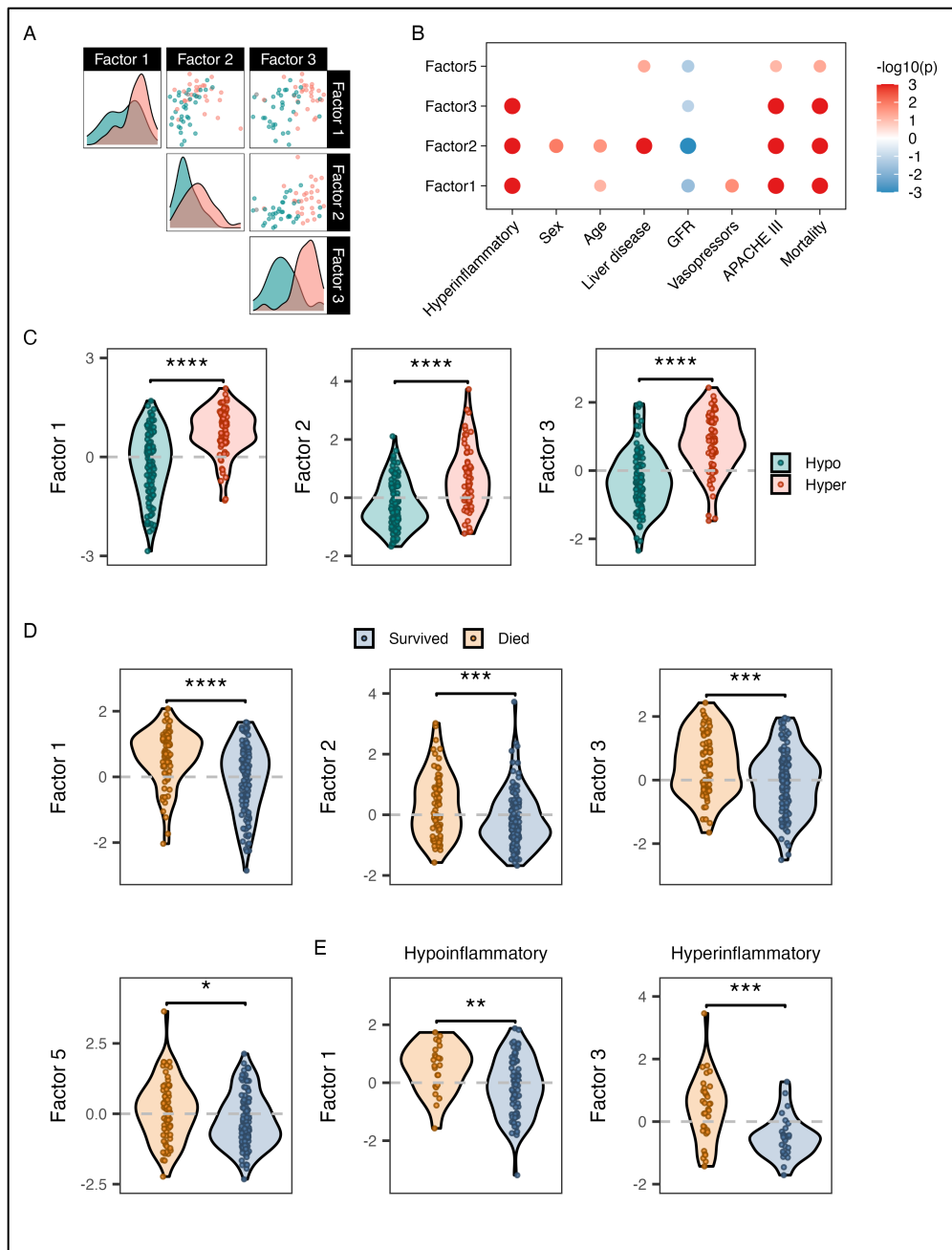
1048 (E) Top genes in Factor 1 by relative scaled weight. (F) Enriched gene expression pathways in
1049 Factor 1. X-axis depicts normalized enrichment score (NES). NMD = nonsense-mediated decay.
1050 APACHE = Acute Physiology and Chronic Health Evaluation III score; BMI = body mass index;
1051 GFR = glomerular filtration rate; IL = interleukin; metab = metabolite; Neut = neutrophil; NMB
1052 = neuromuscular blockade; NMD = nonsense mediated decay; PFRatio = PaO₂:FiO₂ at the time
1053 of enrollment; TCR = T cell receptor; VFD = ventilator free days
1054



1056

1057 **Figure 7. Hyperinflammatory MEFISTO and mortality-associated signature.** Analysis of
 1058 137 samples from 80 patients at two timepoints. **(A)** Proportion of total variance explained per
 1059 data modality (gene, metabolite). **(B)** Proportion of total variance explained per MEFISTO
 1060 factor. **(C)** Association of MEFISTO factors with clinical variables at Day 0 as determined via
 1061 Spearman’s correlation for continuous predictors and linear regression for categorical predictors

1062 (FDR <0.05). **(D)** The slope of change in factor 3 over time by 90-day mortality. P-value derived
1063 from interaction term of a linear mixed effects regression model with 90-day mortality, timepoint
1064 and their interaction as fixed effects and patient as random effect. **(E)** Top genes in Factor 3 by
1065 relative scaled weight. **(F)** Top metabolites in Factor 3 by relative scaled weight. **(G)** Top
1066 enriched gene expression pathways by normalized enrichment score (NES) in Factor 3. **(H)** Top
1067 enriched metabolic pathways by NES in Factor 3. ESR: estrogen receptor; LC: long chain;
1068 metab: metabolism; MUFA: monounsaturated fatty acid; plt: platelet; PUFA: polyunsaturated
1069 fatty acid. Sat: saturated. APACHE = Acute Physiology and Chronic Health Evaluation III score;
1070 BMI = body mass index; Carn = carnitine; FA = fatty acid; GFR = glomerular filtration rate;
1071 HSC = hematopoietic stem cell; LC = long chain; metab = metabolism; MUFA =
1072 monounsaturated fatty acid; PUFA = polyunsaturated fatty acid; Sat = saturated



1073

1074 **Figure 8. ROSE MEFISTO factor projections in the EARLI observational cohort. (A)**

1075 Scatterplot of paired projected factor values per patient sample, colored by LCA phenotype

1076 designation, in patients with both transcriptomic and metabolomic data available (N = 61). **(B)**

1077 Association of projected MEFISTO factor values with clinical variables as determined via

1078 Spearman's correlation for continuous predictors and linear regression for categorical predictors.

1079 (C) Projected factor values per patient sample comparing Hyperinflammatory to
1080 Hypoinflammatory phenotype. P-value determined by Wilcoxon rank sum. N = 189 patients with
1081 transcriptomic data (Factors 1 and 3), and N = 183 patients with metabolomic data (Factor 2).
1082 (D) Projected factor values per patient sample comparing hospital survivors to non-survivors in
1083 those with physician-adjudicated sepsis and transcriptomic data (N = 196 for transcriptomic
1084 Factors 1, 3, and 5; N = 195 for metabolomic Factor 2). P-value determined by Wilcoxon rank-
1085 sum. (E) Projected phenotype-specific MEFISTO factors associated with mortality onto the
1086 extreme ($p > 0.9$) Hypoinflammatory (left, N = 101) and extreme Hyperinflammatory (right, N =
1087 61) patients in EARLI. APACHE = Acute Physiology and Chronic Health Evaluation III score;
1088 GFR = glomerular filtration rate. *: $p \leq 0.05$, **: $p \leq 0.01$, ***: $p \leq 0.001$, ****: $p \leq 0.0001$